Probing the epoch of reionization with 21cm and metal absorption

A Thesis

submitted to
Indian Institute of Science Education and Research Pune
in partial fulfillment of the requirements for the
BS-MS Dual Degree Programme

by

Aniket Bhagwat

Indian Institute of Science Education and Research Pune
Dr. Homi Bhabha Road,
Pashan, Pune 411008, INDIA.

April, 2019

Supervisor:

Certificate

This is to certify that this dissertation entitled Probing the epoch of reionization with 21cm and metal absorptiontowards the partial fulfilment of the BS-MS dual degree programme at the Indian Institute of Science Education and Research, Pune represents study/work carried out by Aniket Bhagwatat Indian Institute of Science Education and Research under the supervision of , , Department of Physics , during the academic year 2018-2019.

Committee:

Dr. Bhas Bapat

This thesis is dedicated to my parents and my brother for their continued support and love.

Declaration

I hereby declare that the matter embodied in the report entitled Probing the epoch of reionization with 21cm and metal absorption are the results of the work carried out by me at the Department of Physics, Indian Institute of Science Education and Research, Pune, under the supervision of and the same has not been submitted elsewhere for any other degree.

Aniket Bhagwat

Acknowledgments

I would first like to thank Dr. Benedetta Ciardi, who gave me the opportunity to pursue my project work with her group at the Max Planck Institute for Astrophysics, Garching. I am truly grateful for her counsel and mentorship throughout the duration of this work. My sincere thanks to the members of my group : Marius Berg Eide, Philip Busch, Martin Glatzle and Enrico Garaldi for all their help and useful discussions through the course of my project.

I also thank Dr. Bhas Bapat for guiding me as my TAC member and offering assistance in every form. I would like to express my gratitude to Dr. Bhas Bapat and the MS Thesis committee at the Indian Institute of Science Education and Research, Pune, for allowing me to pursue my MS thesis at the Max Planck Institute for Astrophysics, Garching. IISER Pune has provided me with great scientific opportunities for which I am truly grateful.

Special thanks to my friends - Perikles Okalides, Abhijeet Anand, Ricard Adverol, Matteo Frigo, Jere Kuuttila, Vlas Sokolov and Linda Baronchelli and Spandan Choudhury for the interesting conversations over lunch, coffee, at friday WAW beers and the amiable atmosphere at work. Also, I am truly thankful for my friends at IISER who, having been in the same boat as me, continued to help and support me in the most crucial times.

Lastly, I thank my parents and my brother for all their support and encouragement that has made it possible for me to pursue my academic goals.

Abstract

The epoch over which the first luminous sources ionized the neutral hydrogen in the intergalactic medium (IGM) and ended the cosmic dark ages is called as the Epoch of Reionization (EoR). Answering the questions : how and when did reionization occur are key goals of modern day observational and theoretical cosmology. Measurements of the thompson scattering optical depths from observations of the cosmic microwave background and detection and studies of the Gunn-Peterson troughs in the spectra of high redshift quasars have established that reionization occured by z$\approx$ 6. The epoch of reionization has witnessed the birth of the first stars, the initial enrichment of the cosmic gas with metals synthesized in the stars, and the formation of galaxies, including the progenitors of more massive galaxies like the one we line in, the Milky Way and thus is a key epoch in the history of the universe. Imaging the Universe during its infancy remains one of the exciting challenges facing modern cosmology. Determining when and how the first luminous sources reionized the intergalactic medium (IGM) will shed light on both the nature of the first objects and the history of baryonic matter in the universe. Quasar absorption lines play a unique role by probing the properties of diffuse gas on a variety of scales ranging from galactic to intergalactic. Using a suite of radiation-hydrodynamical simulations of galaxy formation and the epoch of reionization called the Aurora simulations, I aim to study correlations between 21 cm and metal absorption a way to probe the properties of the IGM during the EoR.

Contents

List of Figures

List of Tables

Chapter 1

Introduction

1.1 The infant universe

One of the most studied and exciting fields of research in astrophysics is structure formation in our universe, how the highly complex objects around us today grew out of the simple and smooth medium that emerged from the Big Bang. In the last few decades, we have seen remarkable progress in understanding the evolution of structure in the universe, and the basic paradigm for structure formation is now established. Microscopic ($\sim 10^{-5}$) density fluctuations that are observed in the cosmic microwave background (CMB) grew via gravitational instability and they collapsed into the large scale structure that we see today.
The established theory has been very successful in explaining observations of both the early Universe and structures observed in the local universe. But two major epochs remain relatively unknown : we have yet to directly observe the cosmic dark ages between the last scattering surface of the CMB and the formation of the first luminous sources and we are still in infancy of observations of the era of first light that stretches from the formation of the first luminous sources to full reionization of the intergalactic medium (IGM). These epochs between z$\sim$1000 and z$\sim$6 constitute the next big challenge in observational cosmology, where we can directly study the transition between the linear and nonlinear regimes of gravitational growth. Understand the characteristics of the first stars and quasars and how they influenced the local universe around them. They offer an opportunity to connect our detailed pictures of the early Universe with the galaxies around us today.

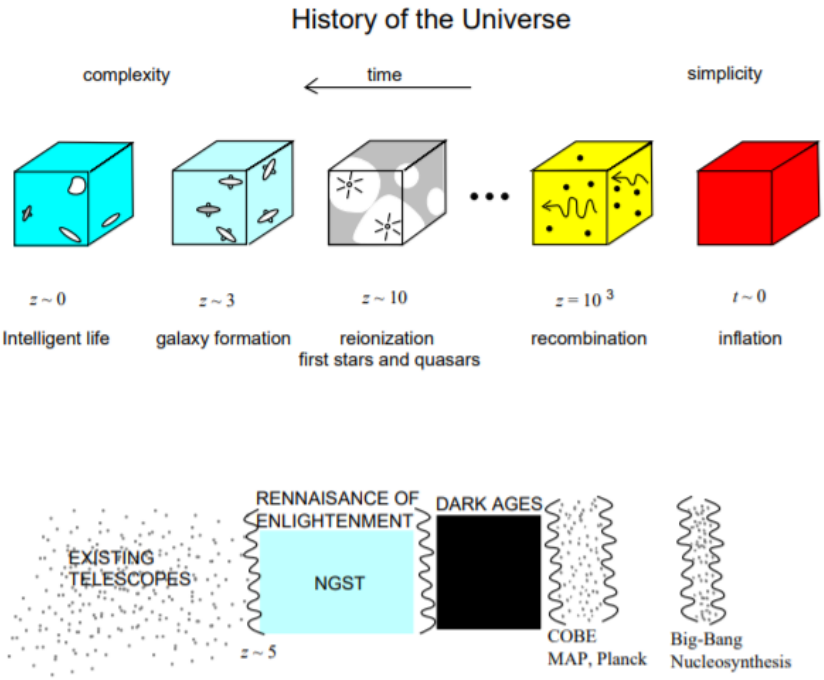

Figure 1.1: Evolution of the universe from a simple state to the complex structure seen today. The cosmic microwave anisotropy experiments ($z \sim 1100$) and the horizon of current observations ($z \sim 5 - 6$). [1]

The detection of cosmic microwave background (CMB) anisotropies confirmed the notion that the large-scale structure in the universe originated from tiny density fluctuations at early times. Due to the natural instability of gravity, the regions that were denser than global average collapsed and formed gravitationally bound objects, first on small spatial scales and then on larger and larger scales. An important outcome of the cosmic microwave anisotropy data is the confirmation that the universe started out simple, it was largely homogeneous and isotropic with small fluctuations that can be described by linear perturbation analysis. The present day universe is clumpy and complicated. Hence, the evolution in time of the universe is the progression from simplicity to complexity.

The formation of the first gravitationally bound objects is the start of the transition from simplicity to complexity. It would seem only natural to attempt to understand the epoch of simplicity before we try to explain the present-day universe (ie. complex). Historically, most of the astronomical studies focused on the local universe to start off with and the study of the early universe has started relatively recently. This deviation was forced upon us by the

lacking state of technology, observation of the high redshift universe requires detection of distant sources, which is feasible only with large telescopes and highly-sensitive instrumentation whose development is recent.

The first luminous sources formed as a consequence of the growth of density fluctuations in the linear regime. They emerge from a well defined set of initial conditions and the physics of their formation can be followed precisely by numerical simulations. The initial conditions are specified by the primordial power spectrum. The mean density of dark matter, initial temperature and densities of the gas and the primordial composition of elements that resulted from the Big-Bang nucleosynthesis. We use these to simulate the evolution of the universe using N-body simulations of dark matter and gas. For the purpose of this project we use such simulations which will be described in a later chapter.

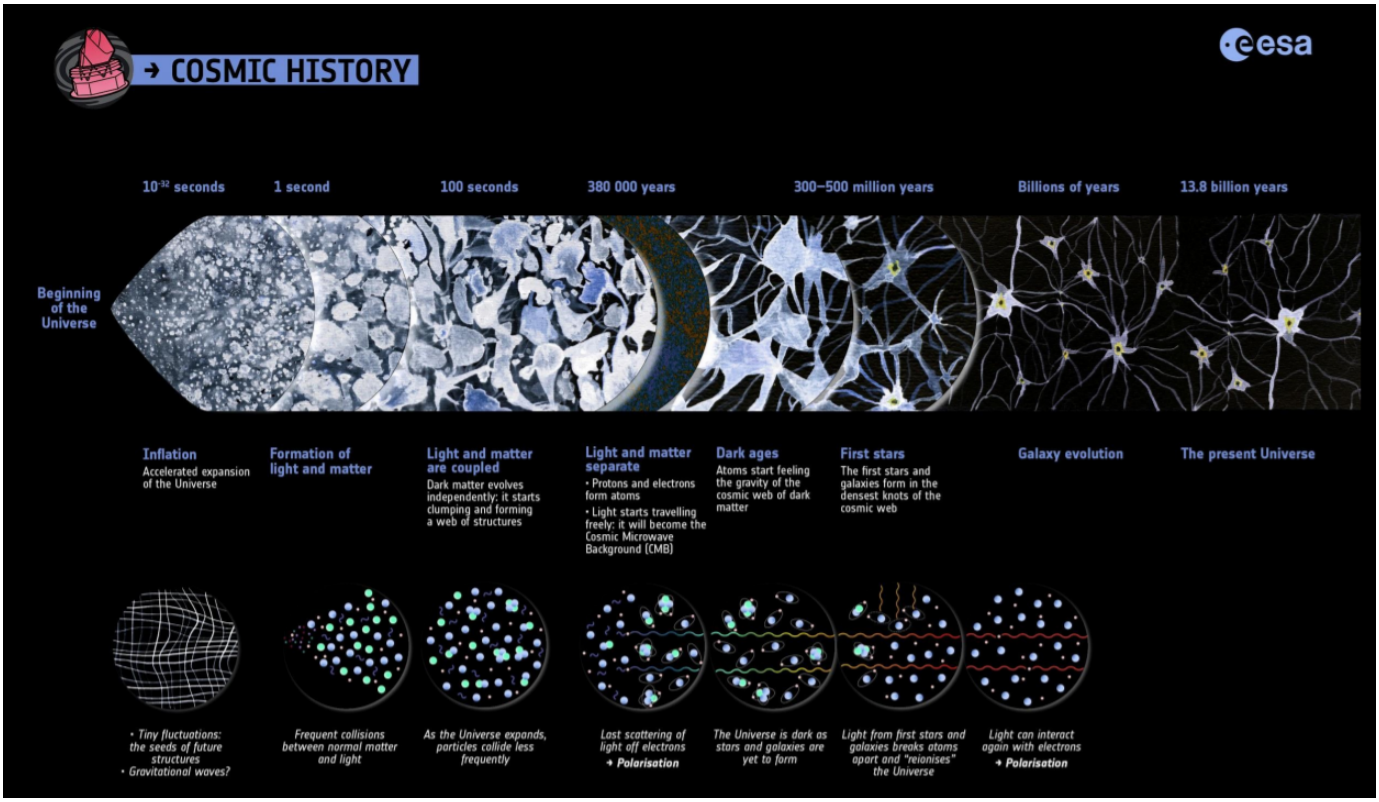

Figure 1.2: Brief history of the universe, describing the various phases. (Picture from ESA)

1.2 Let there be light!

The radiation from first stars and quasars ended the dark ages of the universe and initiated an "age of enlightenment" in the fading glow of the cosmic microwave background. The epoch after the cosmic dark ages, during which the first luminous sources ionized the neutral hydrogen in the intergalactic medium (IGM) is the Epoch of Reionization (EoR). Understanding when and how cosmic reionization occurred is a key goal for observational and theoretical cosmology. Understanding reionization is important for several reasons. First :
1. It impacted most baryonic matter in the universe, a better understanding of the EoR is thus vital for developing a complete picture of the Universes history.
2. Studies of the properties of IGM through reionization will set constraints on properties of the first sources of ionizing radiation and evolution of structure, addressing a broad range of mysteries of the physics of the early Universe.
3. Subsequent galaxy populations are influenced by luminous sources and thus studies of these ionizing sources will help us understand modern day universe better.
The process of the reionization of hydrogen involves several distinct stages. The initial, pre-overlap stage is when isolated luminous sources of ionizing radiation ionize their immediate surroundings. The first galaxies formed in massive halos at which inturn are usually located in highly overdense regions. The ionizing photons that escape from these galaxies have to pass through the surrounding overdense regions, which are characterized by high recombination rates. These ionized regions around ionizing sources usually occur as bubbles called the Strmgren spheres. The egde of these regions spread outward as ionizing radiation propogates through the IGM, this is known as the ionization front. Once the ionizing photons are through the nearby overdense regions, the ionization front propagates more easily into the low-density voids, leaving behind pockets of neutral (due to recombination), high-density gas. At this point, the IGM is a two-phase medium characterized by highly ionized regions separated from neutral regions by ionization fronts. The ionizing intensity is usually very inhomogeneous even within the ionized regions, with the intensity determined by the distance from the nearest source and by the ionizing luminosity of the source. The rapid overlap phase of reionization begins when neighboring HII regions begin to overlap. Whenever two ionized bubbles are joined, each point inside their common boundary becomes exposed to ionizing photons from both sources. Therefore, the ionizing intensity inside HII regions rises rapidly, allowing those regions to expand into high-density gas which had previously recombined fast enough to remain neutral when the ionizing intensity had been low. The overlap of these

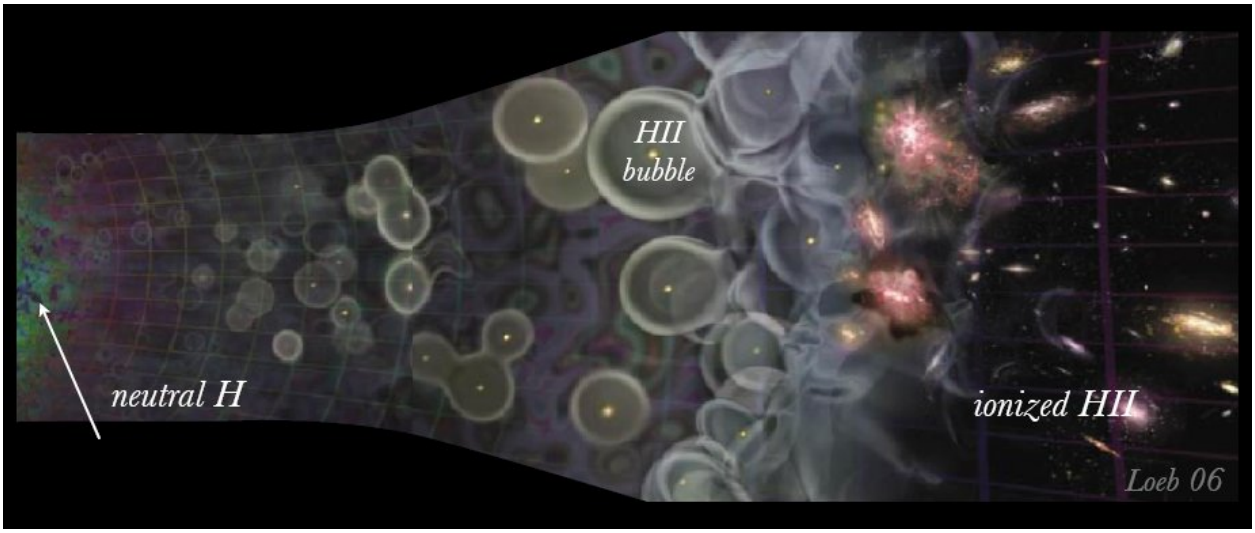

Figure 1.3: The process of reionization: neutral IGM is exposed to ionizing radiation creating HII (ionized hydrogen) bubbles, the bubbles overlap until the universe is completely ionized.

ionized bubbles accelerate the process of reionization, the overlap phase has the character of a phase transition and is expected to occur rapidly, over less than a Hubble time at the overlap redshift. At the end of this stage, most of the IGM is exposed to several unobscured ionizing sources, and therefore the ionizing intensity is much higher than before overlap and it is also much more homogeneous. Another important piece of the puzzle is that hierarchical structure formation models predict a galaxy formation rate that rises rapidly with time at the relevant redshift range. This process leads to a state in which the low-density IGM has been highly ionized and ionizing radiation reaches everywhere except for gas located inside self-shielded, high-density clouds. This marks the end of the overlap phase, and this important landmark is most often referred to as the time of reionization.

1.3 Observational probes of EoR

1.3.1 The lyman α forest

The intergalactic medium (IGM) can be studied through the analysis of the Lyman-α forest which gives us insights about its physical state. This is an absorption phenomenon seen in the spectra of background quasi-stellar objects (QSOs). This phenomenon was first studied

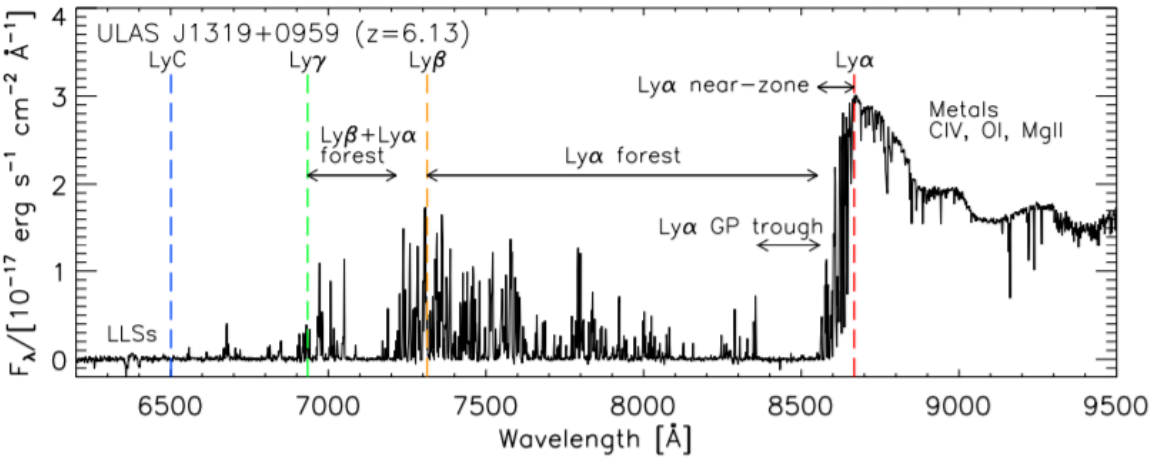

Figure 1.4: Lyman α forest in quasar spectrum of ULAS J1319+0959 at z = 6.13 [2].

in 1965 when a number of studies predicted that an absorption trough will be produced due to neutral hydrogen (later named as the Gunn-Peterson trough) in the spectra of distant QSOs bluewards of the Lyman-α emission line. Gunn & Peterson found a spectral window of reduced flux, and used this measurement to put upper limits on the amount of neutral hydrogen in the intergalactic medium (IGM). Lyman α line has a large absorption cross-section which makes this technique powerful for studying the intergalactic medium. Figure 1.4 hows a typical example of the Lyman-α forest seen in the spectrum of the quasar J1319+0959 at redshift = 6.13 [2]. A unique feature of the lyman-α forest is the density of weak absorption lines which increase with redshift due to the expansion of the Universe. Beyond redshift of around 4, the density of these absorption features becomes so high that one cannot identify separate absorption features. We can only see the flux in between the absorption minima as if they are emission lines rather than absorption lines.

The Lyman α forest is one of the most important tools used to study the IGM properties in its various physical states and has provided us with a wealth of information. It is very sensitive to the neutral hydrogen column density and hence, to the neutral hydrogen fraction as a function of redshift along a line of sight, this can be used to deduce information about the ionization state of IGM along a line of sight. In the section to follow, I briefly describe the basic physics of the Gunn-Peterson trough.

Consider light emitted by a quasar at redshift z_q passing through a uniform IGM with proper neutral hydrogen number density $n_{HI}(z)$. This light is observed at redshift $z < z_q$ with frequency $\nu = \nu_\alpha/(1+z)$, such that the emitted photons have redshifted into Lyα resonance

with the local IGM. The total optical depth along the line of sight is then:

$$\tau_{GP}^{\alpha} = \int_0^{z_q} \sigma_s[\nu(1+z)] n_{HI}(z) \frac{dl}{dz} dz \tag{1.1}$$

where $dl/dz = c/[H(z)(1+z)]$ is the proper line element. Ignoring line broadening effects, the effective scattering cross-section, σ_s, may be approximated by a Dirac delta function peaked at ν_α

$$\sigma_\alpha[\nu(1+z)] = \sigma_\alpha \nu_\alpha \delta[\nu(1+z) - \nu_\alpha] \tag{1.2}$$

where $\sigma_\alpha = 4.48 \times 10^{18} cm^2$ is the Lyα cross-section. Changing the variable of integration to ν, where $dl/d\nu = \lambda\alpha(1+z)/H(z)$ and noting that $\tau_{GP}^{\alpha} = 0$ when $\nu \leq \nu_\alpha/(1+z)$ then yields :

$$\tau_{GP}^{\alpha} \approx \frac{\sigma_\alpha c n_{HI}(z)}{H_0 \Omega_m^{\frac{1}{2}} (1+z)^{\frac{3}{2}}} \tag{1.3}$$

using the high-redshift ($z \geq 2$) approximation for the Hubble parameter, $H(z) \approx H_0 \Omega_m^{\frac{1}{2}} (1+z)^{\frac{3}{2}}$. Identifying $n_{HI} = n_H x_{HI}$ where x_{HI} is the neutral hydrogen fraction, the Gunn-Peterson optical depth at the background density, $\overline{n}_H = \rho_{crit} \Omega_b (1Y)(1+z)^3/m_H$, is then :

$$\tau_{GP}^{\alpha} = 2.3 \times 10^5 x_{HI} \left(\frac{\Omega_b h^2}{0.022}\right) \left(\frac{\Omega_m h^2}{0.142}\right)^{\frac{-1}{2}} \left(\frac{1-Y}{0.76}\right) \left(\frac{1+z}{5}\right)^{\frac{3}{2}} \tag{1.4}$$

where Y is the primordial helium fraction by mass. The transmittance shortward of a quasars Lyα emission line is just $e^{\tau_{GP}^{\alpha}}$. Consequently, even for a modest neutral fraction of $x_{HI} \sim 10^{4.5}$ the Gunn-Peterson optical depth is fully saturated (i.e. $e^{\tau_{GP}^{\alpha}} \approx 0$). Therefore the observations of the Lyα forest implies that intergalactic gas in highly ionized beyond $z \approx 6$ as for the IGM we see today. This is the most reliable and robust evidence that the Universe has in fact reionized.

1.3.2 The cosmic microwave background

The CMB is another probe that provides us with information relevant to the history of reionization. It has been established that the universe recombined into a highly neutral state at z≈1100. If the epoch of recombination did not occur or remained relatively incomplete, that would have resulted a high density of free electrons. This this case, photons couldn't escape Thomson scattering until the density of the universe dropped much further. This scattering

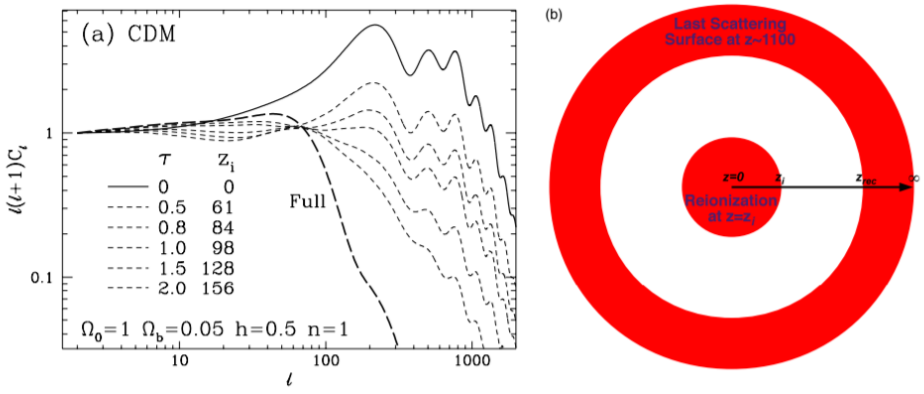

Figure 1.5: Left panel (a): Effect of the epoch of reionization on the CMB temperature angular power spectrum. The effect of the EoR is that it damps anisotropy power as $e^{-2\tau}$ under the horizon scale. All models are fully ionized out to a redshift z_i. With high optical depth, fluctuations at intermediate scales are regenerated as the fully ionized (long-dashed) model shows. Right panel (b) We assume a uniform and sudden reionization history, a change in the reionization redshift, z_i , will translate uniquely to an optical depth for Thomson scattering.

would inevitably destroy the correlations at sub horizon angular scales seen in the CMB data. However, we see these implying that the universe recombined. As reionization started and IGM got more and more ionized, it released free electrons into the IGM. Photons from the CMB can scatter off these free electrons. In order to calculate the effect of reionization on CMB photons, a "visibility function" is used, which is defined as :

$$g(\eta) = -\dot{\tau} e^{-\tau(\eta)} \tag{1.5}$$

where $\eta = \int dt/a$ is the conformal time, a is the scale factore and $\dot{\tau}$ is the 1st derivative of the optical depth with respect to η. The optical depth for Thomson scattering is given by :

$$\tau(\eta) = -\int_{\eta}^{\eta_0} d\eta \dot{\tau} = \int_{\eta}^{\eta_0} d\eta a(\eta) n_e \sigma_T \tag{1.6}$$

, where η_0 is the present time, n_e is the electron density and σ_T is the Thomson cross section. The visibility function gives the probability density that a photon had scattered out of the line of sight between η and $\eta + d\eta$. The influence of reionization on the CMB temperature fluctuations is obtained by integrating equation 1.5 along each line of sight to estimate the temperature fluctuation suppression due to reionization. The suppression probability turns

out to be approximately proportional to $1 - e^{-\tau}$.
The left hand panel of figure 1.5 shows the effect of increasing the value of τ, the Thomson optical depth, on the CMB temperature fluctuation power spectrum. The panel on the right shows the reionization history of the universe assumed in reference to the left panel. Global reionization is assumed to be sudden, therefore there is a one to one correspondence between the thompson scattering optical depth and the redshift of reionization.
using the CMB polarization power spectrum, even more information can be extracted. The polarization of the CMB emerges from the cold dark matter model which say that tiny fluctuations in the early universe grow through gravitational instability into the large scale structure as seen today. The temperature anisotropies seen in the CMB are due to the primordial fluctuations, they would naturally polarize the CMB anisotropies. The degree of linear polarization of the CMB photons at any scale reflects the quadrupole anisotropy in the plasma when they last scattered at the given same scales. From this argument it is clear that the amount of polarization at scales larger than the horizon scale at the last scattering surface should fall down since there is no more coherent quadrupole contribution. The largest scale at which a primordial quadrupole exists is the scale of the horizon at recombination, which roughly is equal to 1° . Hence, any polarization signature observed on scales larger than the horizon scale provides a clear evidence for Thomson scattering at later times when the horizon scale is equivalent to the scale on which polarization has been detected.
The dependence of Thomson scattering cross section on polarization is given by :

$$\frac{d\sigma_T}{d\Omega} = \frac{e^4}{m_e^2 c^4} \mid \epsilon \cdot \epsilon' \mid^2 \tag{1.7}$$

where e and m_e are charge and mass of an electron, $\epsilon \cdot \epsilon'$ is the angle between the incident and scattered photons. The right hand panel of figure 1.6 the process of polarization of the CMB photons due to thomson scattering. If the CMB photons scatter subsequently due to reionization and the incident radiation has a quadrupole moment, then it will be scattered in a polarized manner on the scale roughly equivalent to the horizon scale at the redshift of scattering. Therefore, the scale at which polarization at large scales is detected gives constraints on the redshift of reionization. The presence of large scale correlation in the E-mode is a powerful indication that reionization occured at z≈10. This is a very geometric argument based on the scale of the E-mode power spectrum and the line of sight distance to the onset of reionization front in a given direction. There have been suggestions that we can obtain tighter constrainsts on reionization form the shape of the CMB E-mode polarization

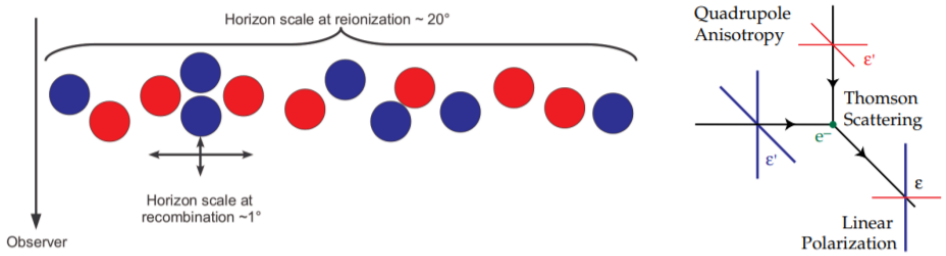

Figure 1.6: Left panel: CMB polarization is sensitive to the quadropole moment of temperature fluctuations. Right panel: Thomson scattering with a quadrupole anisotropy generates linear polarization. The blue is cold and red is hot radiation.

large scale bump. However, large cosmic variance at such large scales limits the amount of information that can be extracted.

From Figure 1.7 we can deduce the optical depth for thomson scattering, τ, caused by the scattering of the CMB photons off free electrons released by reionization to be 0.087±0.017. This could be used as a constraint on the global reionization history through the integral,

$$\tau = \int_0^{z_{dec}} \sigma_T n_e \frac{cH^{-1}dz}{(1+z)\sqrt{\Omega_m(1+z)^3+\Omega_\lambda}} \tag{1.8}$$

where z_{dec} is the decoupling redshift, $_T$ is the Thomson cross section, μ is the mean molecular weight and n_e is the electron density. This integral works both for the optical depth along a single line of sight and also for the mean electron density to get the mean reionization history of the Universe. Better measurements of the τ_T will give us better constraints on when reionization occured.

1.3.3 The 21 cm line of hydrogen

The 21 cm line of neutral hydrogen, in recent years has become of of the most exciting probe of reionization physics. The interaction of the electron and proton spins in the hydrogen atom causes this hyperfine transtition. The excited triplet state is a state in which the spins are parallel whereas the spins at the lower (singlet) state are antiparallel. The 21 cm line is a forbidden line for which the probability for a spontaneous transition ($1 \longrightarrow 0$) is given by the Einstein A coefficient that has the value of $A_{10} = 2.85 \times 10^{-15} s^{-1}$. The Einstein A coefficient

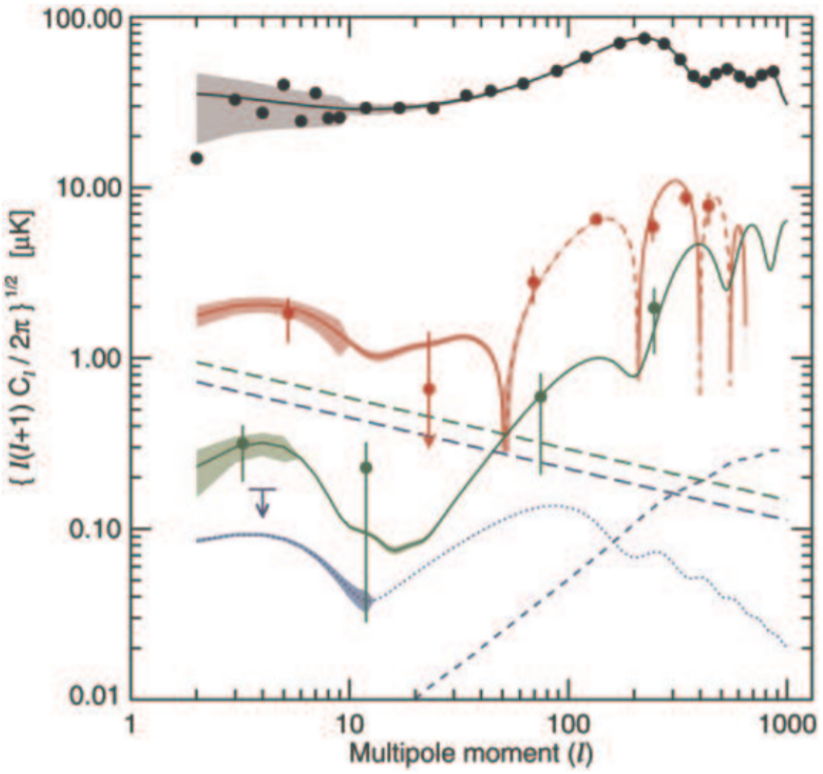

Figure 1.7: Temperature power spectrum and the E-mode polarization cross-power spectrum. (WMAP). TT (black), TE (red), and EE (green) signals for the best fit model. Anticorrelation is suggested by the dashed line for the ET spectrum. TE and EE power spectra show the excess power on large scales caused by reionization.

has a very small value and corresponds to a lifetime of the triplet state of 1.1×10^7 years for spontaneous emission. Despite its low decay rate, the 21 cm transition line is becoming an increasingly important astrophysical probe, simply due to the vast amounts of hydrogen in the universe. In addition to the abundance of neutral hydrogen, collisionional coupling and Lyman-α radiation pumping can establishing the population of the triplet state leading to the hyperfine transition.

1.4 Exploring a new tool to probe reionization?

As mentioned earlier, one of the most common methods of studying the epoch of reionization is the lyman α forest and recent studies have showed that the 21 cm line of neutral hydrogen

is a promising probe with next generation telescopes lined up to detect the same. Metal absorption lines remain relatively understudied through reionization as observations at such high redshift are rare. Only recently with advancements in technology, studies of quasar spectra upto z$\sim$7 are made possible. This opens up a window to study reionization through metal absorption lines. In this thesis, we explore a possible new probe to study the IGM during reionization.

Metal enrichment occurs once star formation starts and processes like supernovae enrich the intergalactic medium (IGM). This usually happens in overdense regions. Neutral hydrogen can remain neutral even in presence of ionizing sources due to recombination and presence of metals can help as some metal species can shield neutral hydrogen from photoionization. If these regions in the IGM do remain largely neutral, we could see absorption features from metals and the 21 cm line of neutral hydrogen (which is sensitive to the neutral hydrogen fraction) in the spectrum of bright background source such as a quasar or even a gamma ray burst. This provides us a with a unique way to study the IGM using absorption lines at high redshifts both theoretically and observationally (through reionization). Using simulations of reionization we study the correlation between the 21 cm absorption and metal absorption to understand the observational feasibility of such a study to probe the EoR.

Chapter 2

Theory

2.1 21 cm line of hydrogen

2.1.1 Physics of the 21 cm line

Hydrogen is the most abundant atomic species in the universe and thus can act a useful tracer of local properties and physical state of gas. The simplicity of its structure: a proton and electron calls into question the richness of the physics involved. The 21 cm line of hydrogen arises from the hyperfine splitting of the 1S ground state as a result of the interaction of the magnetic moments of the proton and the electron. This splitting leads to two distinct energy levels separated by an energy difference of $\delta E = 5.9 \times 10^6$eV. This energy difference corresponding to a wavelength of $\approx$21 cm at a frequency = 1420.4 MHz. This frequency is precisely known from studies of hydrogen masers.

The 21 cm line was first predicted by Van de Hulst in 1942 and has been used as an astrophysical probe since it was first detected by Ewen & Purcell in 1951. In cosmological context the 21 cm line has been used as a probe of gas properties along a line of sight to a background radio source. The observed signal depends on the radiative transfer processes along a given line of sight. Looking at the equation of radiative transfer for the specific intensity $I(\nu)$ (per unit frequency ν) in the absence of scattering along a line of sight (s

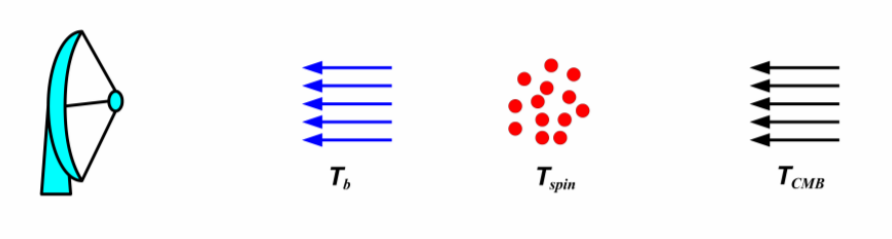

Figure 2.1: Simplistic drawing shows the radiative transfer problem we are describing. We start from the background (CMB) radiation, which passes through a gas cloud with temperature T_{spin} and emerging from the cloud with a temperature T_b that is measured by a telescope.

being the coordinate along the line) :

$$\frac{dI}{ds} = -\alpha_\nu I_\nu + j_\nu \tag{2.1}$$

where absorption and emission coefficients of the intervening gas are α_ν and j_ν respectively. Assuming the Rayleigh-Jeans limit such that $I_\nu = \frac{2k_b T\nu^2}{c^2}$ and writing optical depth τ as $\tau = \int ds\alpha_\nu(s)$, we write eq 2.1 as :

$$T_b^{obs} = T_{ex}(1 - e^{-\tau_\nu}) + T_R(\nu)e^{-\tau_\nu} \tag{2.2}$$

where T_R is the brightness temperature along the line of sight through a cloud of optical depth τ_ν ,T_{ex} is the excitation temperature and T_b is the observed temperature. The excitation temperature of the 21 cm line is also known as the spin temperature T_S. It is defined through the ratio between the number densities n_i of hydrogen atoms in the two hyperfine levels (label with a subscript 0 and 1 for the 1s singlet and 1s triplet levels, respectively)

$$\frac{n_1}{n_0} = (\frac{g_1}{g_0})exp(-\frac{T_*}{T_S}) \tag{2.3}$$

where $(g_1/g_0) = 3$ is the ratio of the statistical degeneracy factors of the two levels, and T_* $= \mathrm{hc/k}\lambda_{21cm} \approx 0.0682$ K. Therefore, the optical depth of a cloud of hydrogen will be :

$$\tau_\nu = \int ds[1 - e^{(\frac{-E_{10}}{k_b T_S})}]\sigma_0\phi(\nu)n_0 \tag{2.4}$$

where $n_0 = n_H/4$ with n_H being the hydrogen density, the 21 cm cross-section is $\sigma(\nu) = sigma_0\phi(\nu)$, $\sigma_0 = \frac{3c^2A_{10}}{8\pi\nu^2}$, $A_{10} = 2.85 \times 10^{-15}s^{-1}$ is the einstein coefficient of the spin-flip transition, and the line profile ($\phi(\nu)$) is normalised so that $\int \phi(\nu)d\nu = 1$.

The key to the detectability of the 21 cm signal depends on the spin temperature. The 21 cm signal will be observable only if the spin temperature deviates from the background temperature. I briefly describe the physics that determines the spin temperature and how spatial variation in the spin temperature conveys information about astrophysical sources.
The spin temperature of the gas is determined by three processes:
(i) Absorption (emission) of 21 cm photons from (to) the background radio source (CMB often used).
(ii) Collisions with other hydrogen atoms ,electrons and protons. (Collisional coupling).
(iii) Resonant scattering of Lyα photons that cause a spin flip via an intermediate excited state. (Ly α pumping).
The rate of these processes is fast compared to the deexcitation time of the spinflip line, therefore to a good approximation the spin temperature is determined by an equilibrium balance of the 3 processes. In this limit, the spin temperature is given by :

$$T_S^{-1} = \frac{T_\gamma^{-1} + x_\alpha T_c^{-1} + x_c T_K^{-1}}{1 + x_\alpha + x_c} \tag{2.5}$$

where T_γ is the temperature of the surrounding bath of radio photons, typically set by the CMB so that $T_\gamma = T_{CMB}$, T_α is the color temperature of the Lyα radiation field at the Lyα frequency and is closely coupled to the gas kinetic temperature T_K by recoil during repeated scattering, x_c, x_α are the coupling coefficients due to atomic collisions and scattering of Lyα photons, respectively.
There are two typical background radio sources that are important for the 21 cm line as a probe of astrophysics. The CMB may be used as a radio background source, if so, $T_R = T_{CMB}$ and the 21 cm feature is seen as a spectral distortion to the CMB blackbody at appropriate radio frequencies. The other situation is when one uses a radio loud source (ex. radio loud quasar) as the background. In this case, the background source will always be much brighter than the weak emission from diffuse hydrogen gas ($T_R \gg T_S$) therefore, the diffuse gas is seen in absorption against the background source. As a result absorption lines can be seen from regions of neutral gas at different distances to the source leads to a "forest of lines known as the "21cm forest which is analogous to the Lyα forest. Depending on the brightness of

the background source, the 21 cm forest can be studied with high frequency resolution to probing small scale structures(kpc sized) in the IGM.

2.1.2 Collisional coupling

Collisions between different particles may induce spin-flips in a hydrogen atom and dominate the coupling in the early universe where the gas density is high and collisions can occur more frequently. There are three main channels that occur: collisions between two hydrogen atoms, collisions between a hydrogen atom an electron or collisions between a hydrogen atom and a proton. The collisional coupling for a species i is :

$$x_c^i = \frac{C_{10}T_*}{A_{10}T_\gamma} = \frac{n_i k_{10}^i}{A_{10}}\frac{T_*}{T_\gamma} \tag{2.6}$$

where C_{10} is the collisional excitation rate, k_{10}^i is the specific rate coefficient for spin deexcitation by collisions with species i (in $cm^3 s^{-1}$). This process is relevant during the cosmic dark ages when the coupling is dominated by collisional coupling. Collisional coupling can lead to a suppression of the 21 cm signal.

2.1.3 Wouthuysen-Field effect

The observations planned for the 21 cm line are for redshifts at which collisional coupling of the 21 cm line is inefficient. From the onset of star formation, resonant scattering of the Ly α photons can provide another channel for coupling. This phenomenon is known as the Wouthuysen-Field effect illustrated in figure 2.2 which shows the hyperfine structure of the hydrogen (1s and 2p levels). If we assume that hydrogen is initially in the hyperfine singlet state, absorption of a Lyα photon will excite the atom into either of the central 2p hyperfine states (Dipole selection rules allow : ΔF = 0, 1 , no F = 0 $\longrightarrow$ 0 make the other two hyperfine levels inaccessible). The emission of a Lyα photon from this intermediate state can relax the hydrogen atom to either of the two ground state hyperfine levels. If the relaxed atom ends up in the triplet state, a spinflip has occured. Via this process, the resonant scattering of Lyα photons can produce a spin-flip.

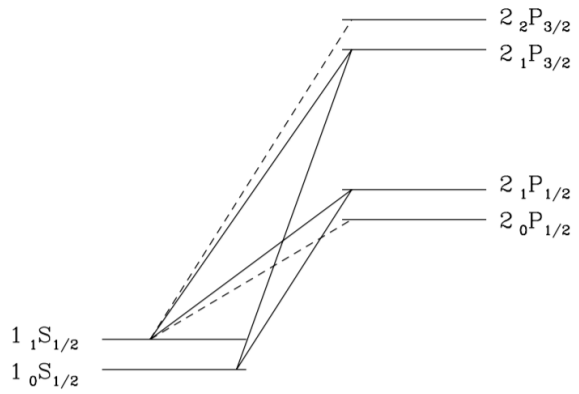

Figure 2.2: Hyperfine structure of the hydrogen atom shpwing the atomic transitions relevant for the Wouthuysen-Field effect. Solid line transitions allow spin flips, while dashed transitions are allowed but do not contribute to spin flips.

I will in brief describe the physics governing this effect. Writing the coupling coefficient as :

$$x_\alpha = \frac{4P_\alpha}{27A_{10}}\frac{T_*}{T_\gamma} \tag{2.7}$$

where P_α is the scattering rate of Lyα photons. The scattering rate between the two hyperfine levels is related to P_α as $P_{01} = 4P_\alpha$ / 27, which is a result from atomic physics and assumes a constant radiation field.
The scattering rate of Lyα photons from a hydrogen atom is given by :

$$P_\alpha = 4\pi\chi_\alpha \int d\nu J_\nu(\nu)\phi_\alpha(\nu) \tag{2.8}$$

where $\sigma_\nu = \chi_\alpha\phi_\alpha(\nu)$ the local absorption cross section, $\chi_\alpha \approx (\pi e^2/m_e c)f_\alpha$ is the oscillation strength of the Lyα transition, $\phi_\alpha(\nu)$ is the Lyα absorption profile, and $J_\alpha(\nu)$ is the angle-averaged specific intensity of the background radiation field.
We can then write the coupling coefficient as :

$$x_\alpha = \frac{16\pi^2 T_* e^2 f_\alpha}{27A_{10}T_\gamma m_e c}S_\alpha J_\alpha \tag{2.9}$$

where J_α is the specific flux evaluated at the Lyα frequency. $S_\alpha = \int dx\phi_\alpha(x)J_\nu(x)/J_{\rm inf}$, with $J_{\rm inf}$ being the flux away from the absorption feature, as a correction factor (order

of unity) to describe the detailed structure of the photon distribution in the neighborhood of the Lyα resonance. Equation 2.9 can be used to calculate the critical flux required to produce $x_\alpha = S_\alpha$ by rewriting it as $x_\alpha = S_\alpha J_\alpha / J_\alpha^C$ where $J_\alpha^C = 1.165 \times 10^{10}[(1+z)/20]$ $cm^{-2}Hz^{-1}sr^{-1}$. This condition is usually satisfied when star formation starts.

The physics described above couples the spin temperature to the colour temperature of the radiation field, which is a measure of the shape of the radiation field as a function of frequency around the Lyα line defined by :

$$\frac{h}{k_B T_c} = -\frac{dlogn_\nu}{d\nu} \tag{2.10}$$

where $n_\nu = c^2 J_\nu / 2\nu^2$ is the photon occupation number. Typically, $T_C = T_K$, as in most cases the optical depth to Lyα scattering is very large leading to a large number of scatterings of Lyα photons. This results in a local equilibrium setting between the radiation field and the gas for frequencies near the line center. This occurs through the scattering Lyα photons around the frequencies of the Lyα resonance which is seen as a feature in the frequency distribution of photons. Expansion of the universe causes redshifting which leads to a flow of photons from high to low frequency at a given rate. This leads to a flow of photons into Lyα resonance and these may be scattered to either larger or smaller frequencies and since the scattering cross section is symmetric, the rate of flow to be preserved. However, every scattering event will cause the lyα photon to lose a fraction of its energy $h\nu/m_p c^2$ due to the recoil of the atom. The loss of energy leads to an increased flow to lower energies leaving a deficit close to the line center. This process creates the feature as scattering shuffles the distribution of photons leading to an asymmetry about the line. This asymmetry is what is required to bring the distribution into local thermal equilibrium ($T_C = T_K$).

The shape of this feature determines S_α and since recoils cause an absorption feature, this ensures $S_\alpha \leq 1$. The recoil has most effect at lower temperatures leading to the suppression of the Wouthuysen effect. In cases where the IGM is warm/hot, this suppression is negligible. In the phenomena we study, the are interested in photons redshifting into the Lyα resonance from below the Lyα resonance frequency. Lyα photons can also be produced through atomic cascades from photons redshifting into higher Lyman series resonances. Such processes that contribute to the amplification Lyα flux through redistribution can contribute to the Wouthuysen-Field coupling.

The description above dives into the subtleties that go into to determining the strength of the Lyα coupling. These processes can modulate the 21 cm signal.

2.1.4 The 21 cm forest

Studies of the 21 cm line have primarily used the CMB as a backlight but another important case is where absorption from the 21 cm line is seen in the spectra of background radio loud quasars. First attempts to study extragalactic 21 cm absorption lines were using a background radio loud quasar. The absorption spectra are expected to show a "forest" of absorption lines due to absorption in clouds of neutral hydrogen along lines of sights and these spectra have been labeled as the "21cm forests" analogous to the Lyα forest.

The Lyα forest is observed at redshifts $z \leq 6$, when the universe is mostly ionized, the 21 cm forest will be seen at higher redshifts when the universe has a high neutral hydrogen fraction. The 21 cm line usually occurs in the optically thin region implying it won't saturate, the 21 cm forest can be used to study detailed properties of the IGM. The Lyman-α forest and the 21 cm forest probe very different physical states of the IGM hence together can be used to probe the evolution of the IGM.
The 21 cm forest differs from the emission signal of the diffuse medium in a number of ways. The brightness temperature of radio loud quasars is typically $\approx 10^{11\sim12}K$ implying that the 21 cm line is always seen in absorption against the source. The strength of the absorption feature depends upon the 21 cm optical depth. The 21 cm optical depth of a cloud of neutral hydrogen located at redshift z along the line of sight can be written as [23]:

$$\begin{aligned}\tau_{21\mathrm{cm}} &= \frac{3}{32\pi}\frac{hc^3A_{10}}{k_B{\nu_{21\mathrm{cm}}}^2}(1+z)^{\frac{3}{2}}\frac{n_{HI}}{T_k}\left(1+\frac{1}{H(z)}\frac{dv_{||}}{dl}\right)^{-1} \\ &\approx 0.0088(1+z)^{\frac{3}{2}}\frac{(1+\delta)x_{\mathrm{HI}}}{T_k}\left(1+\frac{1}{H(z)}\frac{dv_{||}}{dl}\right)^{-1}\end{aligned} \tag{2.11}$$

where $A_{10} = 2.85 \times 10^{-15}s^{-1}$ is the einstein coefficient of the corresponding hyperfine transition, $H(z)$ is the hubble parameter, n_{HI} is the local neutral hydrogen number density, T_S is the local hydrogen spin temperature, δ is the local baryon overdensity and x_{HI} is the local neutral hydrogen fraction. Finally, $\frac{dv_{||}}{dl}$ is the peculiar velocity gradient along the line of sight, with $dv_{||}$ and dl both in proper or comoving units. The other symbols appearing in the equation have the standard meaning adopted in literature. We make the common assumption that $(1 + \frac{1}{H(z)}\frac{dv_{||}}{dl}) \sim 1$ and that the spin temperature is coupled to the kinetic temperature of the gas.
We see from this expression that the optical depth depends primarily upon the neutral hy-

drogen fraction and spin temperature of gas. The optical depth is maximized for a fully neutral and cold IGM. As the IGM is heated and becomes hotter, the 21 cm signature will survive only in highly neutral regions. The 21 cm forest may show several distinct features:
(ii) Variations on small scales in the intensity due to fluctuations in the density, neutral fraction and temperature of the IGM along the line of sight
(iii) Transmission windows due to photoionized bubbles along a line of sight
(iv) Absorption features which are deep arising from dense neutral hydrogen clouds.
The evolution of the 21 cm optical depth depends on the spin temperature of gas and its neutral hydrogen fraction, at high redshifts when the IGM is mostly neutral and the evolution is dictated by the spin temperature. T_S rises from ≈10 K to ≈ 10^4K by the end of reionization, causing τ_0 to fall by several orders of magnitude due to heating alone. Also, as reionization proceeds, the neutral hydrogen fraction drops from $x_{HI} = 1$ to the $x_{HI} \approx 10^{-4}$ as seen in the Lyα forest, the optical depth drops even further. Therefore, tracing the evolution of the mean optical depth would provide a useful constraint on the thermal evolution of the IGM. The 21 cm forest hence opens up a window to study the physical properties of the IGM and its evolution through reionization.

2.2 Metal absorption systems

Metal absorption lines combined with the Lyα forest act as key probes of the high-redshift universe. These two systems reflect the chemical enrichment and ionization state of gas in the regions in and around galaxies. The abundance of metals gives us an idea about the history of global star formation. The number densities, ionic ratios and absorption profiles of metal absorbers contain information on the mechanisms that lead to metal pollution in the IGM, the stellar populations that produced the metals and the ionization state of the metal rich gas. Metal absorption lines are a very useful tool to study galaxies from the lower end of the luminosity functions as we very well may detect the metal absorption lines from these galaxies which are not detected by large scale surveys. Metal absorption systems are viable even at very high redshift as they can be detected even when hydrogen is completely saturated in the spectra of the background quasars, since some of these transitions occur redward of Lyα and are thus unaffected by Gunn-Peterson troughs and hence are very observable.

2.2.1 Absorption systems

In this project we studied specific metal absorption systems of interest. Observational studies of metal absorption systems in the tail end of reionization have focused on typically 3 types of metal absorbers:

- High ionization state systems traced by metal lines like C IV and Si IV refered to these as the C IV systems.
- Low ionization state systems traced by metal lines like O I, C II, Si II and Fe II refered to as O I systems.
- Variable ionization state systems traced by metal lines like Mg II refered to as Mg II systems.

Most of the work done previously carried out on metal absorption is done at redshifts post reionization or in the tail end of reionization (z$\sim$6). In this project we study metal absorption from some of these absorption systems through reionization ie. z = 11 $\sim$ 6. I will briefly describe these systems in the following sections.

2.2.2 O I systems

Low-ionization metal lines are potentially powerful probes of the high-redshift Universe. They trace the dense gas in and around galaxies, offering insights into the interstellar medium of these objects analogous to the ways in which damped Lyα absorbers (DLAs) trace properties of galaxies at much lower redshifts (e.g. [28]). Since the metals in these absorption systems are often dominated by a single ionization state, determining abundances is relatively straightforward. If the regions of the IGM that remain highly neutral are metal rich, they may give rise to a forest of absorption lines such as OI and C II that can be detected in quasar spectra (ex. [11], [7]).
Metal-enriched gas where the hydrogen is largely neutral is traced by lines such as O I, C II, S II, and Fe II. O I is particularly useful for studying neutral gas since the ionization potential of oxygen and hydrogen are very similar ($\Delta E = 0.19eV$) therefore, they can exist

in tight charge exchange equilibrium over a wide range of physical conditions ([12]). :

$$\begin{aligned} O + H^+ &\longrightarrow O^+ + H \\ O^+ + H &\longrightarrow O + H^+ \end{aligned} \tag{2.12}$$

Metal species where the ionization potential is significantly less than 13.6eV are usually not shielded by atomic hydrogen and occur in their lower ionization states in a predominantly neutral gas. At z$\leq$5, low-ionization systems are typically found by their strong, often damped, hydrogen Lyα lines. At higher redshifts, the Lyα forest is more and more saturated which makes identifying individual Lyα absorbers difficult, therefore metal systems must be identified using pseudo multiplets of lines redward of Lyα, such as O I (λ1302), C II (λ1334), and S II (λ1260, λ1304, and λ1526). Since these low ionization states have been suggested to occur in neutral hydrogen, where the 21 cm absorption signal will be high, we can use a combination of these to trace metal rich HI regions through reionization.

2.2.3 C IV systems

The C IV doublet is a commonly used absorption line tracer of metals (especially at low redshifts). The C IV line is highly sensitive to metal rich ionized gas. This absorption line offers many advantages that make its observational detection easier than other metal species. It has a large oscillator strength, a wavelength redward of Lyα emission and a doublet transition. Since these systems of higher ionization states have a higher ionization potentials, are likely to occur in regions where hydrogen is highly ionized and could be potentially used as tracers for H II regions at high redshifts.

2.2.4 Mg II systems

Last but not the least the Mg II doublet absorption line systems can be used to trace both neutral and ionized gas phases. The column densities of strong Mg II systems are quite hard to measure as this line can be saturated. This system is therefore studied in terms of the rest-frame equivalent width of the absorption line.

Chapter 3

Numerical Simulations

Developing a better understanding of the physics that drove reionization of the universe is one of the primary goals of modern day astrophysics. An important question that is being studied is whether the ionizing radiation from stars was sufficient to accomplish reionization, or if there were other sources at play (such as quasars, blackholes etc.). Upcoming observations from next generation of telescopes with, e.g., ALMA([13]), MUSE([27]) and JWST ([6]), LOFAR ([29]), MWA ([9]) and SKA ([10]), will shed further light on these issues.
Theoretical modelling and studies of the early universe and studies of reionization will be critical to interpreting data from these telescopes. A powerful tool to build theoretical models is running cosmological radiative transfer (RT) simulations of the epoch of reionzation. These simulations track the gravitational growth of density fluctuations in the expanding Universe and the hydrodynamical evolution of the cosmic gas, include recipes for star formation and the associated feedback, and also follow the propagation of ionizing radiation. Most such simulations are modelled carefully with a scientific goal in mind as these are computationally expensive (take weeks to run). I used the Aurora simulations modelled and run by Andreas Pawlik et. al. [15] to study the IGM during reionization.

3.1 Aurora Simulations

In this work I used Aurora, a suite of cosmological radiation-hydrodynamical Smoothed Particle Hydrodynamics (SPH) simulations of galaxy formation and reionization. The Aurora

simulation	L_{box} (h^{-1} cMpc)	N_{DM}	m_{DM}	m_{gas}	ϵ_{soft} (h^{-1} ckpc)
L025N0512	25.0	512^3	1.00×10^7	2.04×10^6	1.95
L012N0256	12.5	256^3	1.00×10^7	2.04×10^6	1.95
L012N0512	12.5	512^3	1.25×10^6	2.55×10^5	0.98
L025N0256	25.0	256^3	8.20×10^7	1.63×10^7	3.91
L050N0512	50.0	512^3	8.20×10^7	1.63×10^7	3.91
L100N1024	100.0	1024^3	8.20×10^7	1.63×10^7	3.91

Table 3.1: Parameters used in the suite of the Aurora simulations: simulation name; comoving size of the simulation box (L_{box}); number of DM particles (N_{DM}); mass of dark matter particles (m_{DM}); initial mass of gas particles (m_{gas}); gravitational softening length (ϵ_{soft})

simulations track the formation of stars and galaxies at high resolution across cosmological scales, and also follow the hydrodynamically coupled transport of ionizing radiation from stars, supernovae (SNe) and the enrichment of the universe with metals. In this section I will briefly describe the simulations used and I invite the reader to refer the original paper [15] for more details. Table 3.1 gives the simulation parameters for the suite of simultaions. The ΛCDM cosmological model is used with parameters Ω_m= 0.265, Ω_b= 0.0448 and Ω_Λ = 0.735, $n_s = 0.963$, $\sigma_8 = 0.801$, and $h = 0.71$ [8], consistent with the most recent constraints from observations of the CMB by the Planck satellite [18]. Figure 3.1 shows a slice from the simulation showing a slice of the neutral hydrogen fraction and a zoomed in version of part of the same slice. This figure was taken directly from [15].

3.1.1 Hydrodynamics and Radiative transfer

For hydrodynamics, aurora uses a modified version of the N-body/TreePM Smoothed Particle Hydrodynamics (SPH) code GADGET ([24]). The simulations start at z= 127 and are run down to z=6. Radiative transport (RT) in a simulation box is a very expensive process computationally. Aurora tackles this by using the spatially adaptive radiation transport technique TRAPHIC ([16, 17, 14, 19]) that solves multiscale problems efficiently. The computational time used by TRAPHIC is independent of the number of radiation sources. The spatial adaptive resolution for evolution of gas and transport of ionizing radiation is kept the same. The ionizing radiation is coupled hydrodynamically to the evolution of the gas, which accurately accounts for feedback from photoheating.

3.1.2 Chemistry and star formation

Aurora follows the non-equilibrium chemistry and radiative cooling of the gas assuming that the gas is of primordial composition with a hydrogen mass fraction $X = 0.75$ and a helium mass fraction $Y = 1 - X$.
Galactic winds are also accounted for that are driven by star formation and the enrichment of the gas with metals synthesized in the stars. Aurora uses the pressure-dependent model of [21] as the sub-grid prescription for star formation. Stellar evolution assumes a [3] initial mass function and determines the element-by-element gas enrichment [26], the rates of supernova events, and stellar ionizing luminosities [20]. Stellar feedback is implemented thermally following the stochastic method of [4]. Each box is checked so as to match certain observational constraints such as the evolution of star formation rate density, star formation rates, the neutral hydrogen fraction, the photoionization rate at the end of reionization.

3.1.3 Chemical Enrichment

Aurora accounts for the age-dependent release of hydrogen, helium, and metals by Type II core-collapse and Type Ia SNe, stellar winds from massive stars and AGB stars ([22] and [26]). The Aurora outputs store the ejected mass of 11 individual elements : H, He, C, N, O, Ne, Mg, Si, and Fe. In this project we study absorption from metal systems of interest.

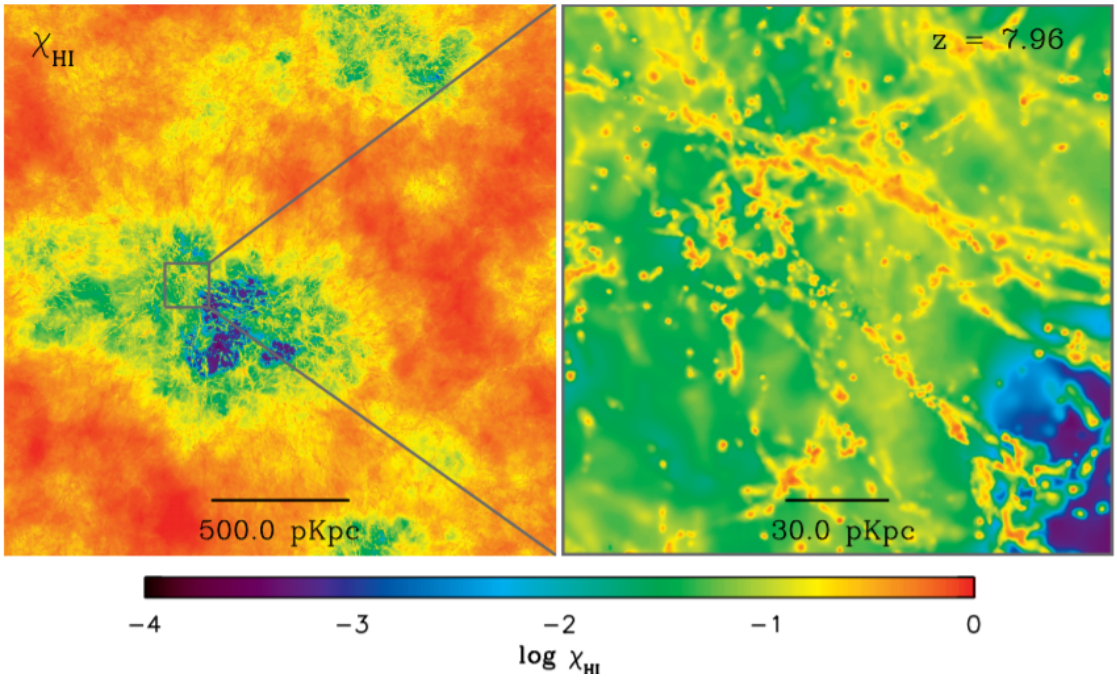

Figure 3.1: The neutral hydrogen fraction at $z \approx 8$ (mean volume-weighted neutral hydrogen fraction of about 0.4) in the high resolution box L012N0512 of size 12.5 h^1 comoving Mpc. Right panel shows a zoomed in region from the left panel and reveals a network of self-shielded and shadowed neutral gaseous objects inside the highly ionized regions. [15]

Chapter 4

Synthetic Spectra

To generate synthetic spectra for both 21 cm and metal absorption, we use the we use the package `Specwizard`, which is based on the implementation described in Appendix A4 of [25]. The code has been modified to use eq. 2.11 to evaluate the 21 cm optical depth. In brief, `Specwizard` evaluates the ionization balance of each particle along a line of sight (LOS) using tables pre-computed with the photoionization package CLOUDY [5] assuming that the gas is exposed to the ionizing UV background seen in the Aurora simulations [15]. This section describes the prescription used by `Specwizard` to calculate these spectra.
We project random lines of sight in the simulation box along the z axis for simplicity, and extract the relevant physical information taking into account positions, velocities, densities and temperatures of the SPH particles inside each line of sight. Subsequently, compute a synthetic spectra in optical depth and flux as a function of the hubble velocity. For a bin j at a position x(j), the density , density weighted temperature and velocity are calculated from:

$$\begin{aligned} \rho_X(j) &= a^3 \sum_i X(i) W_{ij} \\ (\rho T)_X(j) &= a^3 \sum_i X(i) T(i) W_{ij} \\ (\rho v)_X(j) &= a^3 \sum_i X(i)(a\dot{x}(i) + \dot{a}[x(i) - x(j)]) W_{ij} \end{aligned} \tag{4.1}$$

where a is the scale factor, X(i) the abundance of the species X of the SPH particle i and $W_{ij} = mW(q_{ij})/h_{ij}^3$ the normalized SPH kernel. W is the SPH kernel,m the particle mass

and:

$$q_{ij} = \frac{a|x(i) - x(j)|}{h_{ij}}$$
$$h_{ij} = \frac{1}{2}[h(i) + h(j)] \tag{4.2}$$

with h the physical softening scale. Given these quantities, we can calculate number densities and subsequently column density of each ion species in a given velocity bin. The synthetic flux for any transition at the redshift-space coordinate v is given by $F_(v)= e^{-\tau(v)}$, with $\tau(v)$ is given by :

$$\tau(v) = \sqrt{\pi}\frac{e^2}{m_e c^2}\frac{N f \lambda_0}{b} e^{-(u/b)^2} \tag{4.3}$$

where $b = \sqrt{\frac{2k_B T}{m}}$ ie. the doppler width of the line and u is the shift form the line center $u = v(j) - v(k)$, f is the oscillator strength and λ_0 is the rest wavelength of the transition and N is the column density of the ion of interest in the given velocity bin.
The equation above is used for synthetic spectra of metals. For deriving the 21 cm spectra, equation 2.11 is used instead of equation 4.3 with the rest of the procedure being the same.

Chapter 5

Results

5.1 Physical state of the IGM

Figure 5.1 shows maps of the temperature (left panels) and neutral hydrogen fraction (right panels) are shown at redshifts z = 11.32, 7.96 and 6, which correspond to mean H I fractions x_{HI} (gas temperature T) of 0.029, 0.481 and 0.852 (488, 6020 and 10643 K), respectively. We can see the progress of reionization form z = 11.32 to 6. The temperature, at very high redshifts, the universe is cold with a mean temperature of $\sim 10^2$ K with localized regions of very high temperatures $\gg 10^4$ K whereas by the end of reionization, the mean temperature is $\sim 10^4$ K with very localized pockets of very high temperatures $\gg 10^4$ K. If we look at the neutral hydrogen fraction (x_{HI}), the universe goes from highly neutral $x_{HI} \approx 1$ to highly ionized $x_{HI} \approx 10^{-1}$ with localized highly neutral pockets at $z \sim 6$. Figure 5.3 shows the phase diagram of the IGM describing its T and $x_{\rm HI}$ at $z = 11.32$, 7.96 and 6 in overdense and underdense regions. Each panel shows the distribution of all particles in given density state with a given temperature as a function of the neutral hydrogen fraction ($x_{\rm HI}$). Most overdense particles are highly neutral and hot ($\gtrsim 10^4$ K) throughout reionization, although neutral and cold particles are visible at the highest redshift. Such state is predominant also for low density particles, but in this case they persist also at lower redshifts. Most of the underdense particles though have moved to a highly ionized and hot state by the end of reionization. At all redshifts, We see a tail of particles with $T \gg 10^4$, these are the gas particles that are likely shock heated due to energy from stellar feedback/accretion hence

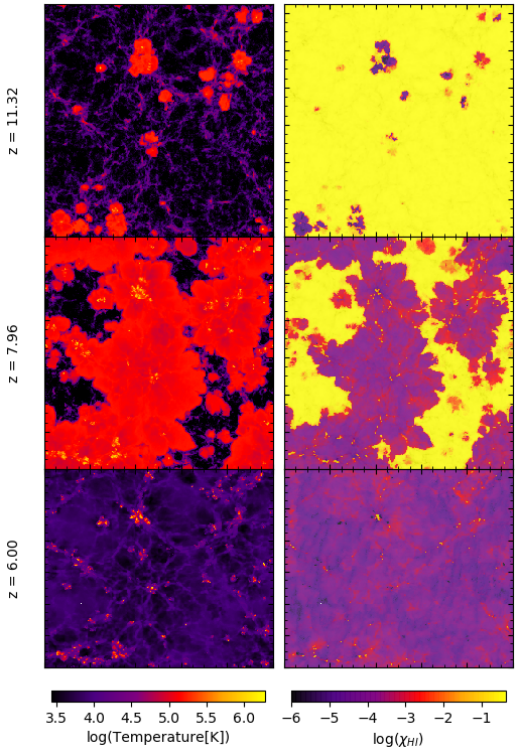

Figure 5.1: *Left panel:* Maps of the temperature at z = 11.32 (top panel), 7.96 (central panel), 6 (lower panel) for the central slice of the simulation box. *Right Panel:* Same as left but for the HI fraction (χ_{HI})

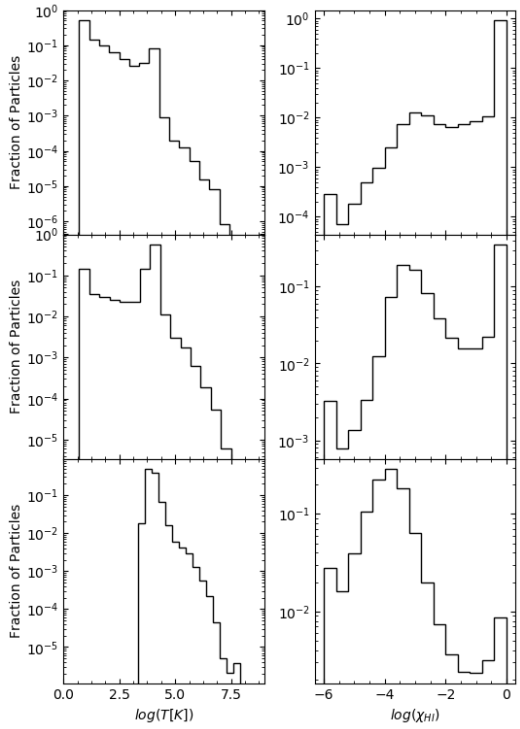

Figure 5.2: *Left panel:* Distribution of the temperature at z = 11.32 (top panel), 7.96 (central panel), 6 (lower panel) for all the gas particles in the simulation box. *Right Panel:* Same as left but for the HI fraction (χ_{HI})

are out of ionization equilibrium and are seen in various physical states ranging from highly neutral to highly ionized. Similarly in figure 5.4, I show a similar phase diagram where the distribution of temperature is shown vs the overdensity for highly neutral and ionized regions, a similar tail of out of equilibrium particles is seen. From these figures we see a qualitative evolution of the IGM through reionization.

The physical state of the IGM is imporant to this study as the physical properties of gas along the projected lines of sight will determine the absorption seen along them. The local gas density determines the column density of the ion of interest and the local gas temperature is of utmost importance to absorption. As seen from earlier sectionsm, the 21 cm optical depth is highly sensitive to the spin temperature (we assume $T_S = T_K$ where T_K is the local gas temperature), and for metal absorption lines, local temperature determines the thermal broadening of the absorpion line. Hence, tracking the qualitaive picture of evolution of IGM

is important as it can give an of how much absorption we may see along lines of sight through the IGM.

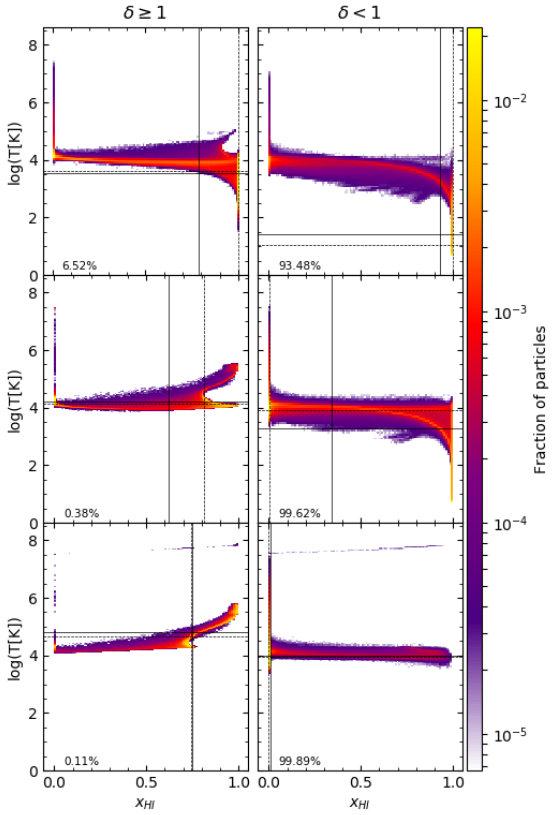

Figure 5.3: Phase diagrams showing the distribution of the IGM at $z = 11.32$ (top panels), 7.96 (middle), 6.0 (bottom) for overdense (left column) and underdense (right) particles. The horizontal solid (dashed) lines indicate the mean (median) temperatures of the particles, while the vertical solid (dashed) lines indicate the mean (median) neutral hydrogen fraction. Percentages in each panel indicate the fraction of particles in an overdense/underdense state.

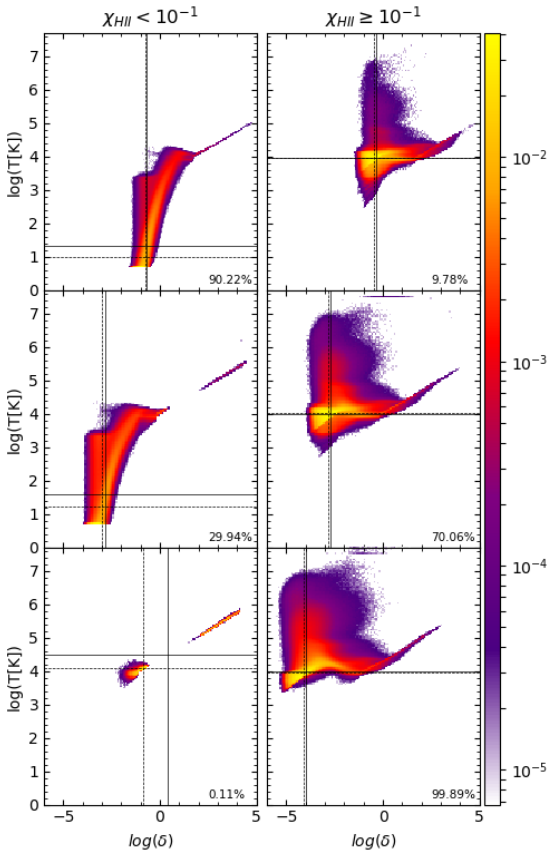

Figure 5.4: Phase diagrams showing the distribution of the IGM at $z = 11.32$ (top panels), 7.96 (middle), 6.0 (bottom) for high neutral (left column) and highly ionized (right) particles. The horizontal solid (dashed) lines indicate the mean (median) temperatures of the particles, while the vertical solid (dashed) lines indicate the mean (median) overdensites. Percentages in each panel indicate the fraction of particles in an neutral/ionized state

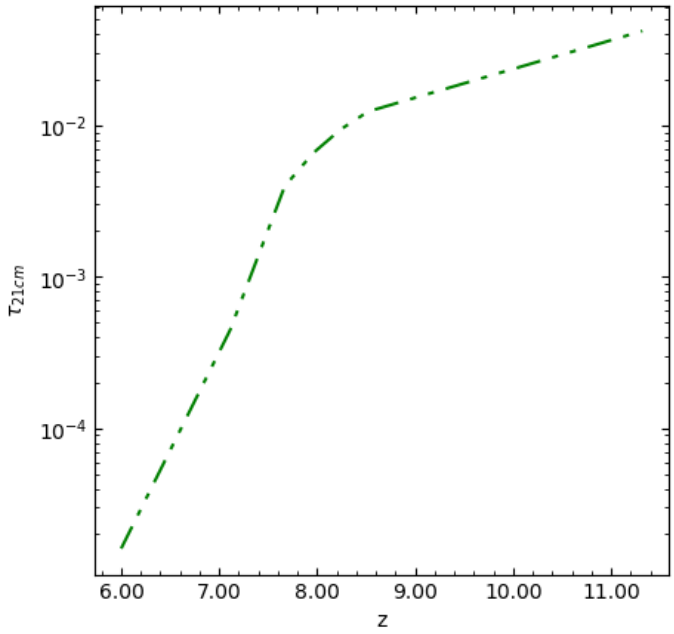

Figure 5.5: Evolution of the volume averaged 21 cm optical depth.

5.2 The 21 cm optical depth

Phase diagrams of the IGM give us an idea of the evolution of the physical state of the IGM. The 21 cm optical depth is affected directly by this evolution as it depends on the local overdensity, temperature and neutral hydrogen fraction. The 21 cm optical depth is calculated as described in the earlier section on the 21 cm forest ([23]). In this section I will describe the statistics of the 21 cm optical depth of all gas particles and its evolution.

Figure 5.5 shows the evolution of the volume averaged optical depth for the 21 cm transition. The volume averaged drops to negligible values towards the end of reionization, this is expected as the IGM is getting highly ionized and hotter.

Although the volume averaged values are very low towards the tail of reionization, figure 5.6 shows that there are significant number of particles with high optical depths. The overdense particles have significantly higher optical depths than the underdense particles. Even at $z = 6$ we see optical depths as high as 0.2 ($e^{-0.2} \approx 0.8$ which would be the transmittance, would produce a big absorption feature!).

We can see that despite of the volume averaged optical depth being very low, there are systems of particles with high optical depth throughout reionization which will can be seen in an absorption spectrum along a line of sight passing though the system.

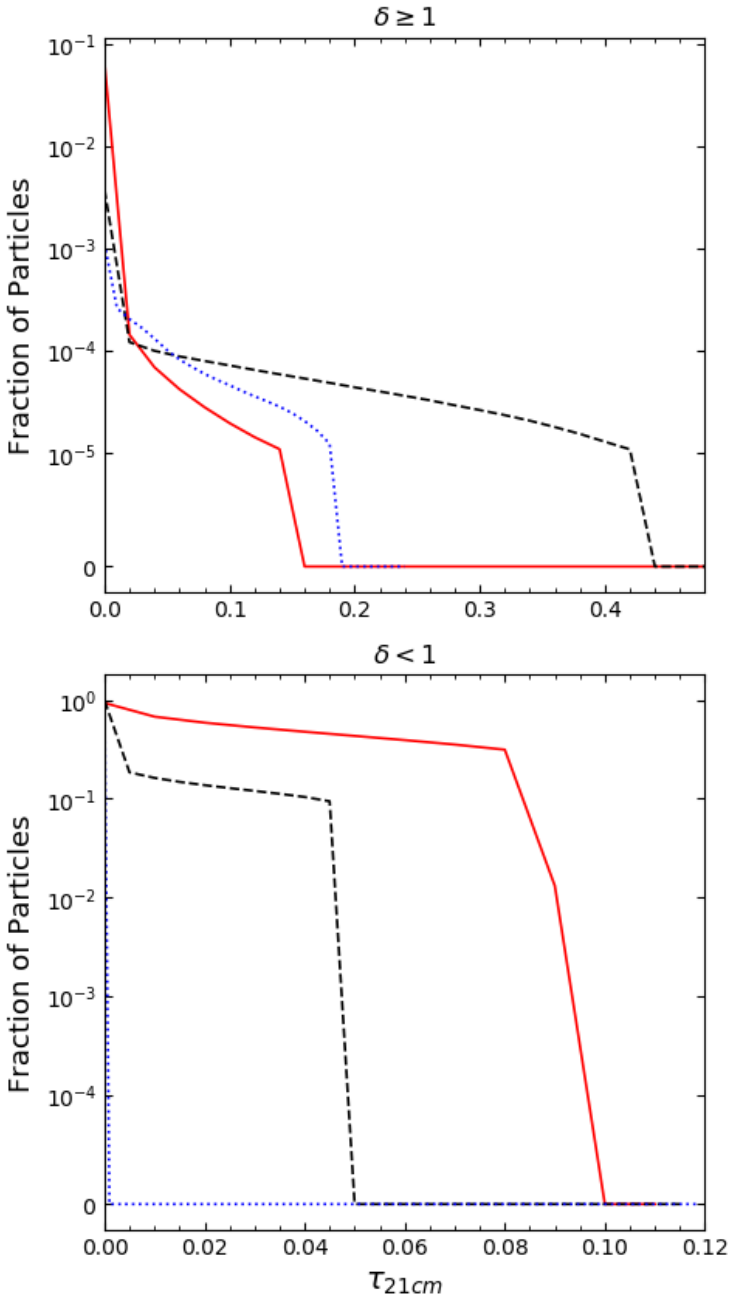

Figure 5.6: A cumulative distribution of 21 cm optical depth (τ_{21cm}) of all gas particles divided by their overdensity. This represents the fraction of particle with optical depths > τ_{21cm} at $z = 11.32$ (red dotted line), 7.96 (black solid) and 6.0 (blue dashed) for overdense and underdense particles.

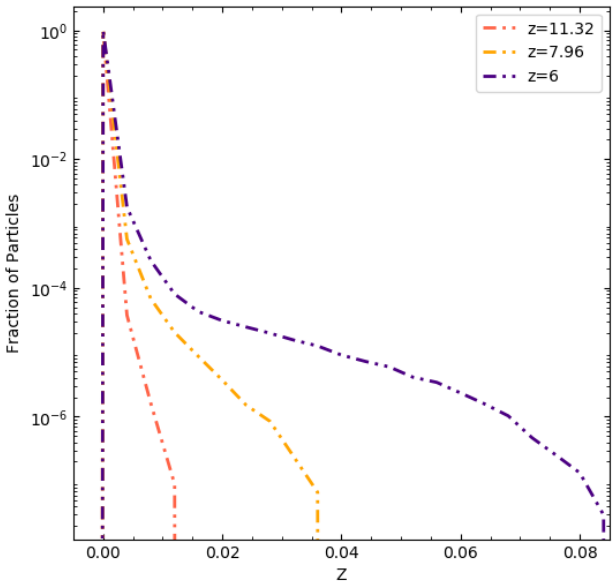

Figure 5.7: Distribution of metallicity of all gas particles at redshifts z = 11.32, 7.96 and 6

5.3 Metal enrichment

One of the most important questions relevant to this study is how high is the metallicity of gas before the end of reionization ie. metal enrichment vs reionization. If the universe is highly metal enriched at high redshifts, it may be used as a very versatile tracer of various properties of the IGM with future observations. Aurora simulations use the chemical enrichment prescription of [26] and trace the individual metaliicities of 11 elements.

The obvious way to look at metal enrichment of IGM is to look at phase diagram of the IGM though reionization with metallicity as the 3rd axis along with looking at the distribution of metallicities of individual gas particles. Figure 5.7 shows the distribution of metallicities of particles through reionization. We see that the IGM is getting more and more metal rich as reionization proceeds and the number of particles polluted by metals also is increasing.

From Figure 5.8, where we show a phase diagram with the metallicity, temperature and neutral hydrogen fraction of particles in the simulation in overdense and underdense regions, we can see that these particles are hot, highly neutral and overdense, while the underdense IGM is hardly enriched with metals. The mean metallicity of overdense particles is in fact 2-3 orders of magnitude higher than underdense particles at any redshift, as indicated by the numbers in each panel.

This phase diagram gives us a wealth of information about the metal rich systems in the

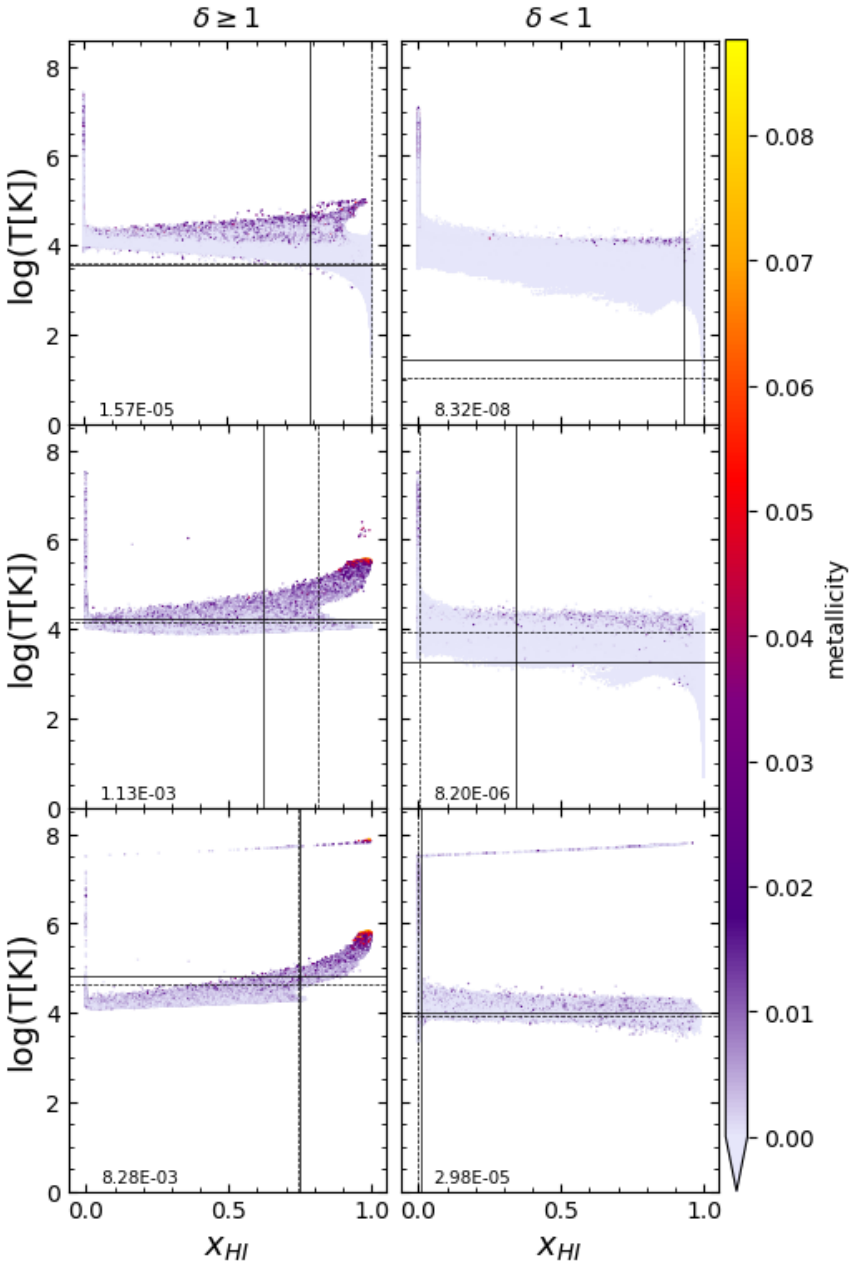

Figure 5.8: Phase diagrams showing the distribution of IGM metallicity as a function of T and $x_{\rm HI}$ at $z = 11.32$ (top panels), 7.96 (middle), 6.0 (bottom) for overdense (left panels) and underdense (right) regions. The horizontal solid (dashed) lines indicate the mean (median) temperatures, while the vertical solid (dashed) lines indicate the mean (median) neutral hydrogen fraction. The colorbar indicates the distribution of metallicity of gas. The numbers in each panel indicates the mean metallicity of the IGM in an overdense/underdense state.

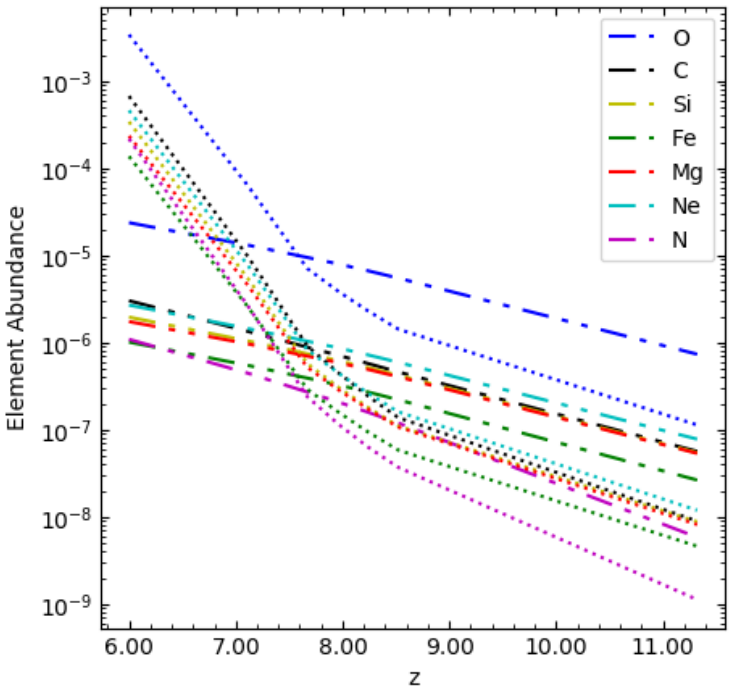

Figure 5.9: Evolution of element abundances of Oxygen, Carbon, Silicon, Iron, Magnesium, Neon and Nitrogen. The dotted lines show mean element abundance of each element as a function of redshift for particles with $\chi_{HI} \geq 0.90$. The dashed lines show the volume averaged abundances for the same elements.

IGM. As seen from the figure, the metal rich portion of the IGM is overdense, very hot ($T \gg 10^4$) and yet it remains highly neutral ($x_{HI} > 0.7$). This indicates that if we look at these specific metal rich systems, it is quite likely that we will see high 21 cm optical depth as well due to the high neutral hydrogen fraction.

Looking at the the evolution of abundances of individual elements through reionization (Figure 5.9), we see that Oxygen is the most abundant followed closely by carbon, neon, silicon magnesium and iron. Oxygen ,carbon and silicon are of importance to this study as they are the most abundant and they have electronic transitions that are observable and have been seen in quasar spectra at lower redshifts. From the same figure, the dotted line represents the element abundances of particles that are almost completely neutral ($x_{HI} > 0.9$). We see a turnover in the dotted line. This could be because of two primary reasons :
(i) At lower redshifts the overdense metal rich regions remain self shielded keeping hydrogen highly neutral.
(ii) At high redshift most of the particles are highly neutral but only a few are metal rich,

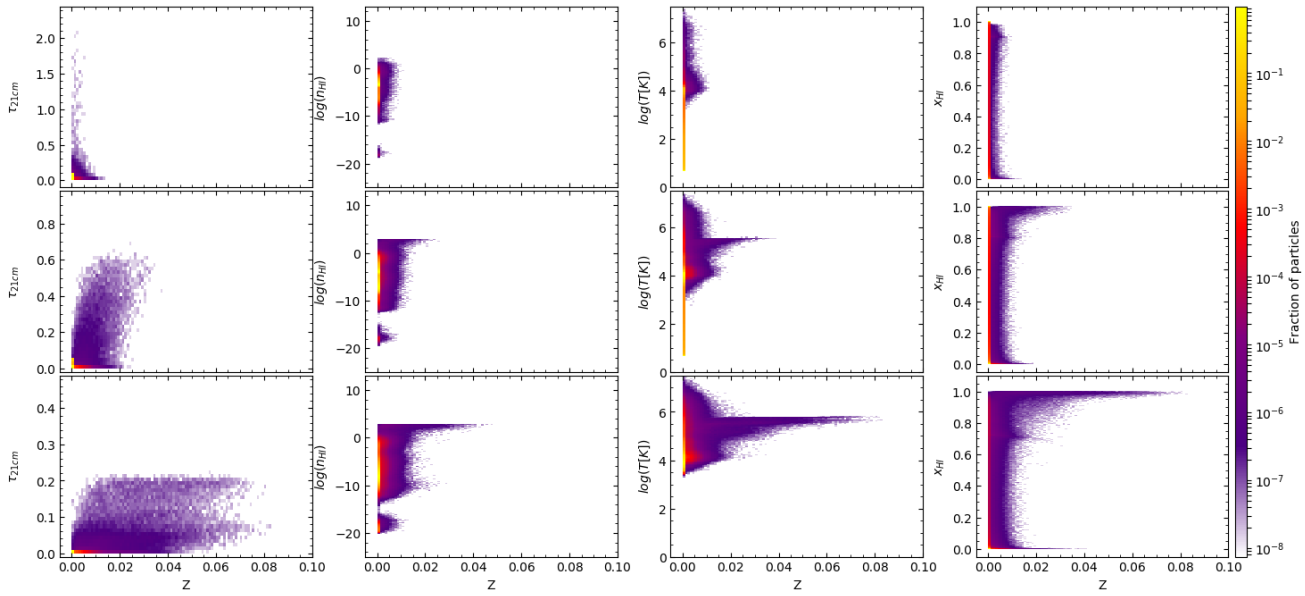

Figure 5.10: Distribution of 21 cm optical depth, hydrogen number density, temperature and neutral hydrogen fraction as a function of the metallicity of gas are shown in columns 1,2 3 and 4 respectively. All results are shown at at $z = 11.32$ (upper panels), 7.96 (middle) and 6 (lower) respectively.

hence the mean metallicity of such particles at high redshifts is expected.

The turnover is seen at $z \sim 8$, that corresponds to a neutral hydrogen fraction of $\sim$0.5.

Figure. 5.10 shows the distribution of various quantities like 21cm optical depth (τ_{21cm}), neutral hydrogen number density (n_{HI}), temperature and neutral hydrogen fraction ($x_{\rm HI}$) as a function of metallicity in columns 1, 2, 3 and 4 respectively at z = 11.32 (upper panels), 7.96 (middle panels) and 6 (lower panels) respectively. From column 1 we see the distribution of τ_{21cm} vs the metallicity of the particles. Throughout reionization we see the diffuse distribution of particles with high metallicity as well as 21 cm optical depth. These are the particles that are of importance to this particular study.

5.4 Absorption spectra

To calculate both metal and 21 cm synthetic absorption spectra, we use the package `Specwizard`, which is based on the implementation described in Appendix A4 of [25] (Described in chapter 4). The code has been modified to use eq. 2.11 to evaluate the 21 cm optical depth.

In brief, `Specwizard` evaluates the ionization balance of each particle along a line of sight (LOS) using tables pre-computed with the photoionization package CLOUDY [5] assuming that the gas is exposed to the ionizing UV background seen in the Aurora simulations [15]. A synthetic spectrum is then computed dividing the LOS into velocity bins and evaluating the optical depth of species i, τ_i, in each bin.

Since our study is at very high redshifts, the number of lines of sight that we will observe will be few even with the next generation of telescopes. We generate 500 random lines of sight. The x and y coordinates for the lines of sight are chosen randomly using a random number generator. Each line of sight is the project along the z-axis and spectrum is calculated along it. The lines of sight are picked randomly so that we don't introduce any bias hence mimicking real life observations.

Along with calculating the 21 cm spectra we calculate the absorption spectra of the following metal lines : `O I, O V, C II, C IV, Si II, Si IV, Fe II, Fe III`. These are a combination of both low ionization state and high ionization state lines (refer to chapter 3). These serve to trace a variety of physical states of the IGM.

Figures 5.11 and 5.12 show samples of synthetic spectra along lines of sight. From top to bottom the panels absorption spectra of 21 cm and O I and some physical characteristics of the gas.

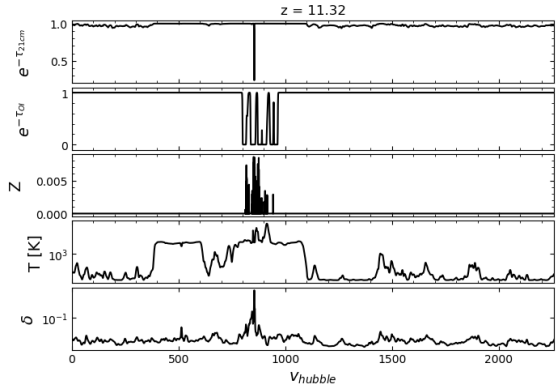

Figure 5.11: Sample line of sight at z = 11.32 showing the 21 cm absorption, the O I absorption, metal mass fraction(metallicity) and temperature along the line of sight.

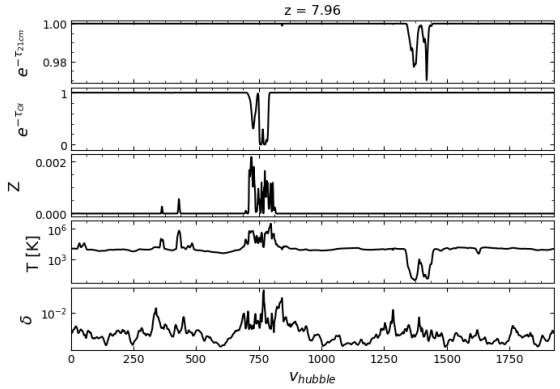

Figure 5.12: Sample line of sight at z = 7.96 showing the 21 cm absorption, the O I absorption, metal mass fraction(metallicity) and temperature along the line of sight.

5.5 Analysis

We created 5000 spectra for each of the metal transitions mentioned above and 21 cm. These are high resolution spectra with a bin width of 1 kms^{-1} with no instrumental or random noise. To analyse these spectra we employ 2 methods, both of which serve to study if metal absorption and 21 cm absorption are correlated through reionization. The analysis is done using the following methodology :

5.5.1 Statistical analysis

We projected 5000 lines of sight and although observations of such a large number of lines of sight at $z \geq 6$ are unlikely at the moment, these can provide us with useful column density and optical depth statistics to study absorption. Figures 5.13 and 5.14 show the distribution of column densities, N (cm^{-2}), of metal ions as a function the column density of neutral hydrogen for metal enriched gas at $z = 11.32$ (top panels), 7.96 (middle), 6.0 (bottom).
As seen from Figure 5.13, the bulk of metal rich gas shifts towards lower values of $N_{\rm HI}$ with decreasing redshift, with a tail of high metal and neutral hydrogen column densities. A similar, but less pronounced, trend is observed for the high ionization state metal lines in Figure 5.14, although in this case the tail is not seen. These high neutral hydrogen column densities do not necessarily translate to high optical depth as $\tau_{\rm 21cm} \propto T_S^{-1}$ (seeFigs. 5.6 and 5.2). Therefore, out of the small fraction of IGM that has high column densities of both low ionization state metals and neutral hydrogen, even fewer will show 21 cm absorption.
In Figs 5.15 and 5.16 we plot $e^{-\tau_{21cm}}$ vs $e^{-\tau_{metal}}$ to see how the column densities translate to absorption features in the synthetic spectra. Plotting $e^{-\tau_{21cm}}$ vs $e^{-\tau_{metal}}$ gives us an idea of how these two quantities depend on each other through the course of reionization. This kind of a study is used as a substitute for equivalent widths of spectral lines. Since metal rich regions are usually hot, the thermal broadening of spectral lines becomes large in these regions, some of the absorption lines are saturated or at times even have damping wings. In such cases, defining the equivalent width of the spectral line becomes difficult. Hence a simple statistical study like described above is usefull to get a quantitative picture of extent of metal and 21 cm absorption in the metal rich IGM.
Figure 5.15 shows the distribution of $e^{-\tau_{21cm}}$ vs $e^{-\tau_{metal}}$ for the lower ionization states of `O I, C II, Si II, Fe II` at z = 11.32 (upper panel), z = 7.96 (middle panel) and z = 6

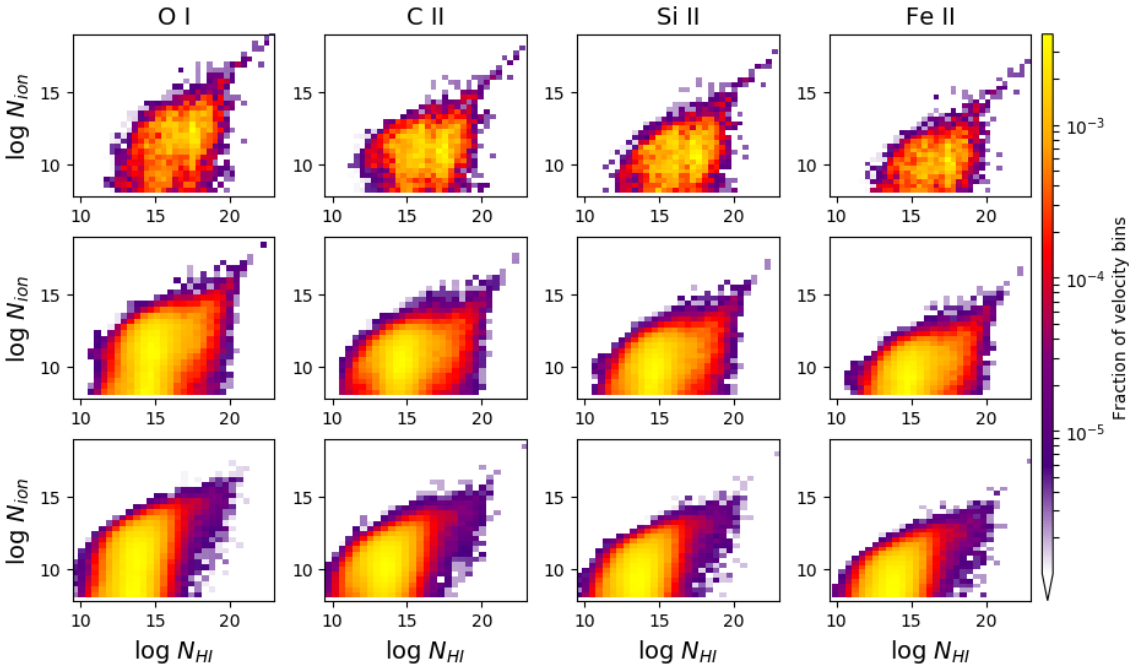

Figure 5.13: Column density (cm^{-2}) of low ionization state metal lines plotted against the column density of neutral hydrogen at $z = 11.32$ (top panels), 7.96 (middle), 6.0 (bottom).

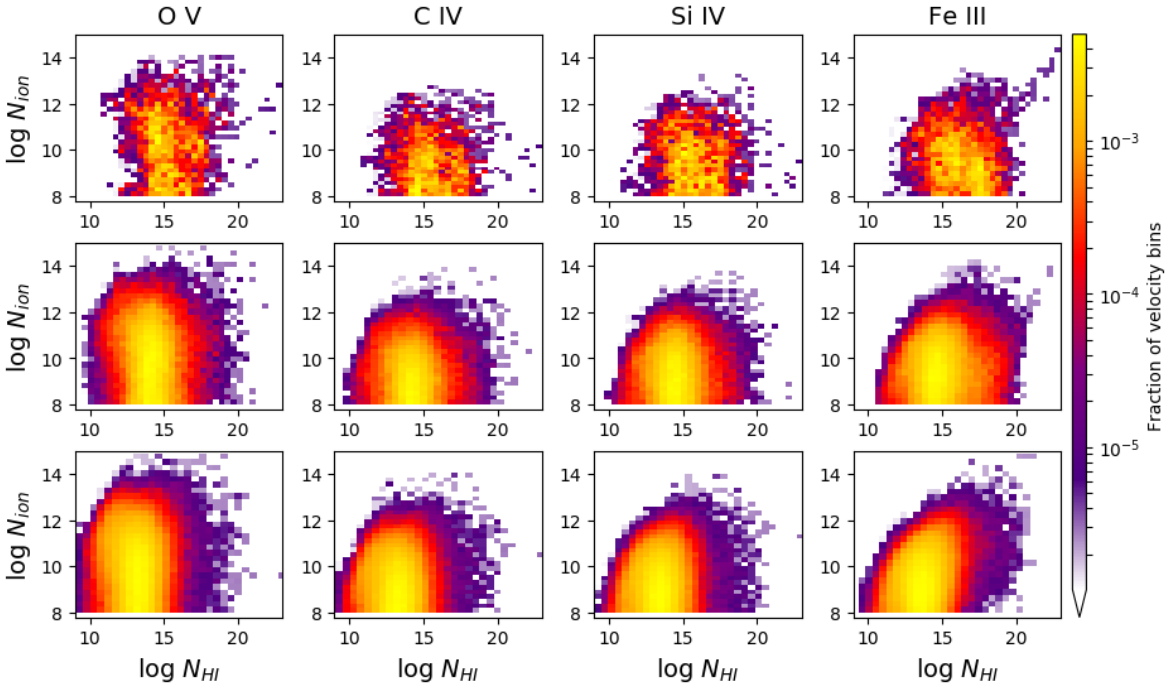

Figure 5.14: Same as above except for high ionization state metals

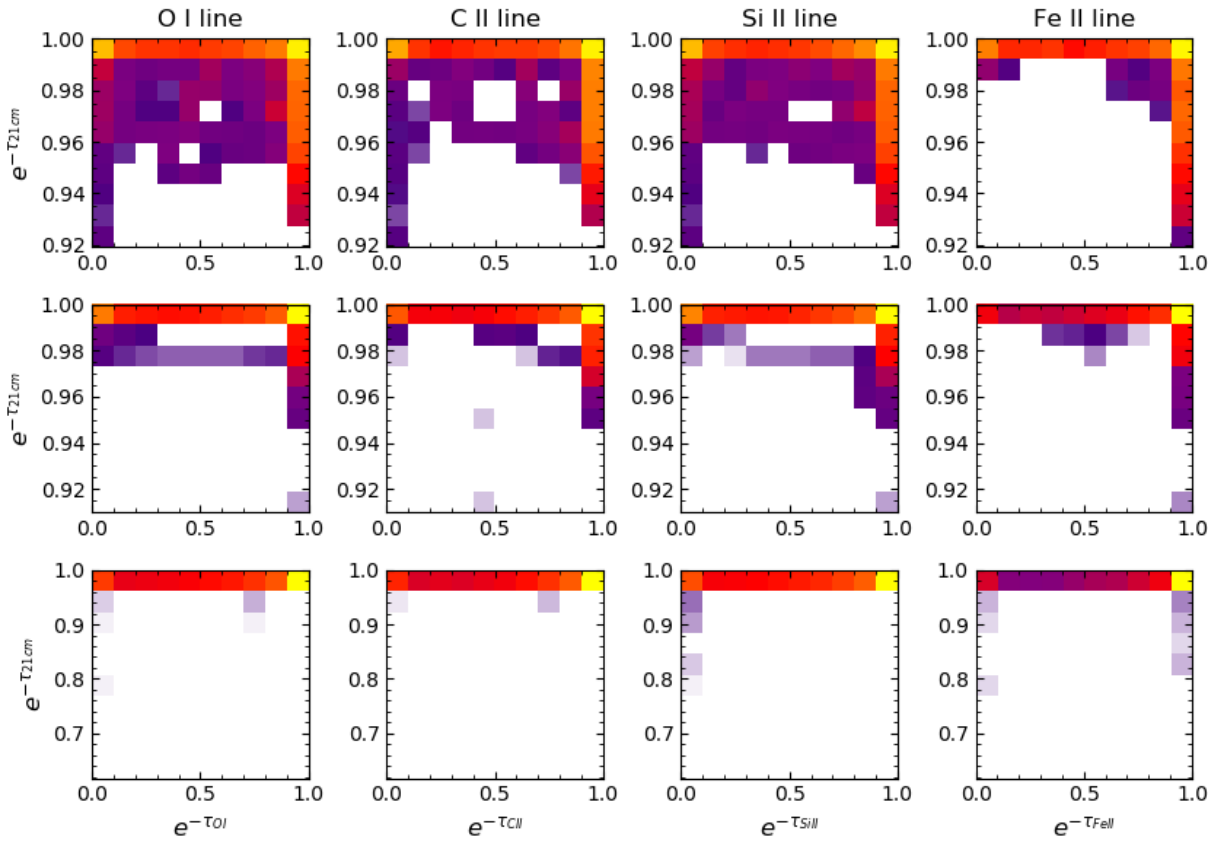

Figure 5.15: τ_{21cm} vs τ_{ions} for low ionization state transitions at z = 11.32 (upper panel), z = 7.96 (middle panel) and z = 6 (lower panels).

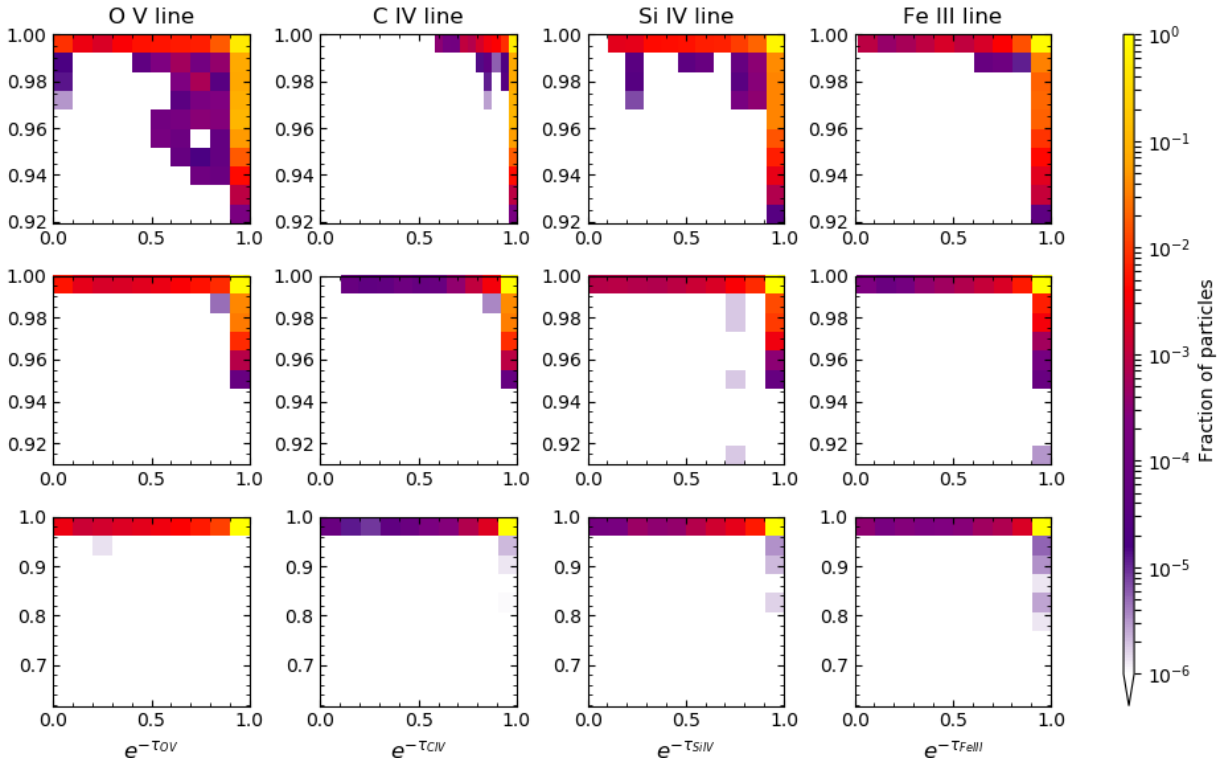

Figure 5.16: τ_{21cm} vs τ_{ions} for high ionization state transitions at z = 11.32 (upper panel), z = 7.96 (middle panel) and z = 6 (lower panels)..

(lower panels). Similarly figure 5.16 shows the distribution of higher ionization states of `O V, C IV, Si IV, Fe III`. Looking at the low ionization states, we see that at z = 11.32 the distribution of particles is quite varied and as reionization proceeds the number of particles shifts toward $e^{\tau_{21cm}} < 0.9$ with the full range of $e^{-\tau_{metal}}$. Most of these lines seem to be saturated at z = 11.32, which means in the absorption spectra these will produce troughs of complete absorption. At all redshifts, the 21 cm optical depths are reasonable, their observability will however depend heavily on the instrument used. Except at $z = 6$ where the 21 cm are high, the absorption features will be quite small and can easily be dominated by noise.

As for the higher ionization states, we see that the absorption from metals is also in the optically thin limit (except O V) ie. absorption lines will not be saturated producing distinct features instead of troughs. We can see that at throughout reionization (especially at $z = 6$) we have significant values of both $e^{-\tau_{21cm}}$ and $e^{-\tau_{metal}}$ for a large number of particles for a study such as this to be observationally viable. If the background source is a very bright source, we can effectively use an absorption study such as this to probe IGM properties.

5.5.2 Stacking

One of the most commonly used technique is stacking of spectra. Keeping in mind the observational constraints on the number of lines of sight that will be available to us from the next generation of telescopes at such high redshifts, we pick randomly 20 lines of sight to stack. Since the spectra are pure ie. noiseless, we do a simple averaging over lines of sight. Figure 5.17 shows the stacked averaged spectrum obtained from stacking 20 lines of sight for low ionization states of metals of interest namely O I, C II, Si II, Fe II. Similarly figure 5.18 shows the same for high ionization states of metals of interest namely O V, C IV, Si IV, Fe III. Both are shown at redshifts z = 11.32 (upper panels), 7.96 (middle panels) and 6 (lower panels). This technique gives us an idea of how a possible noiseless stacking of spectra from a background quasars may look like. It's hard to deduce any correlations by just looking at the spectra from. Hence, we do a 2 point correlation study by cross-correlating the 21 cm absorption spectrum with the metal absorption spectrum. We are running this study by varying the stacking parameters and the results will be available in the near future.

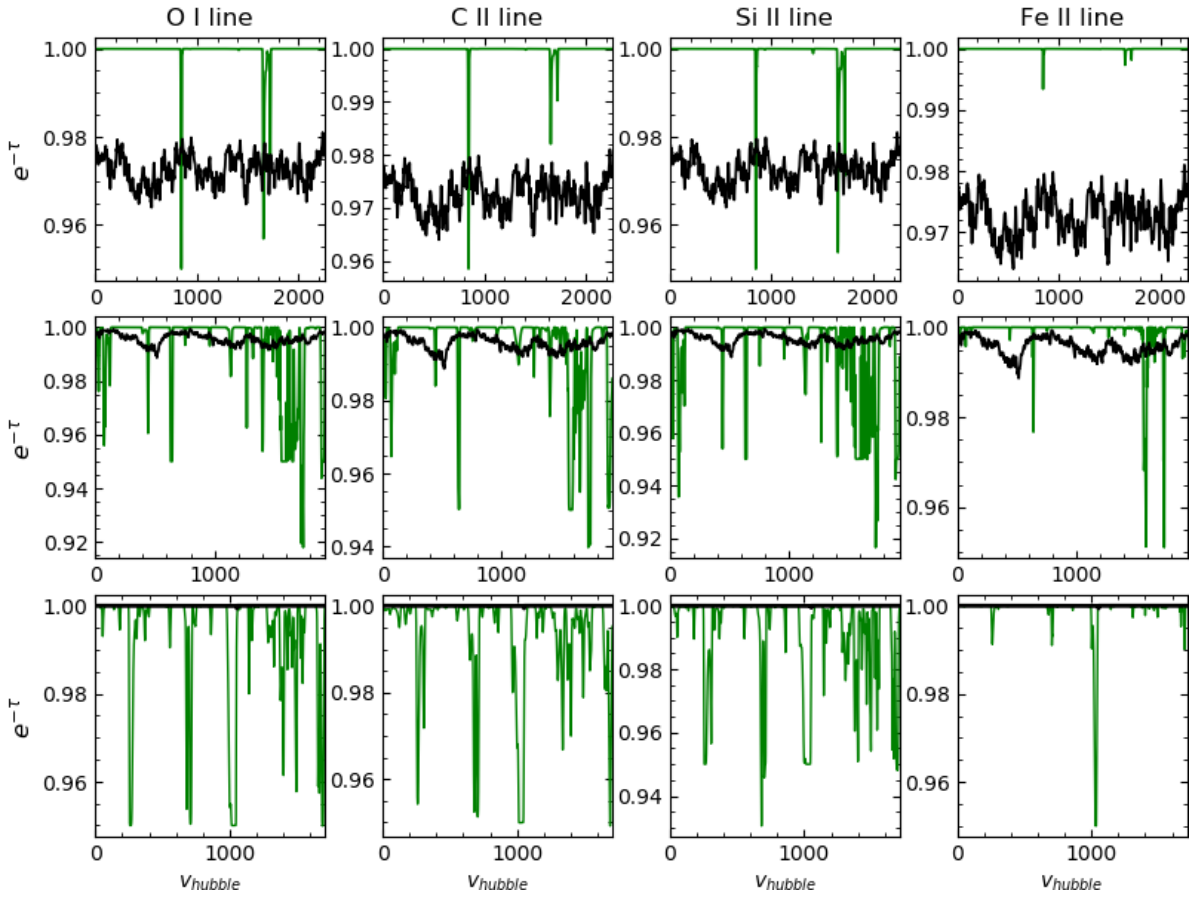

Figure 5.17: Stacked spectra at z = 11.32 (upper panels), 7.96 (middle panels) and 6 (lower panels) for low ionization states of metals specified at the top of the column (green line) and the stacked 21 cm absorpion spectrum (black line).

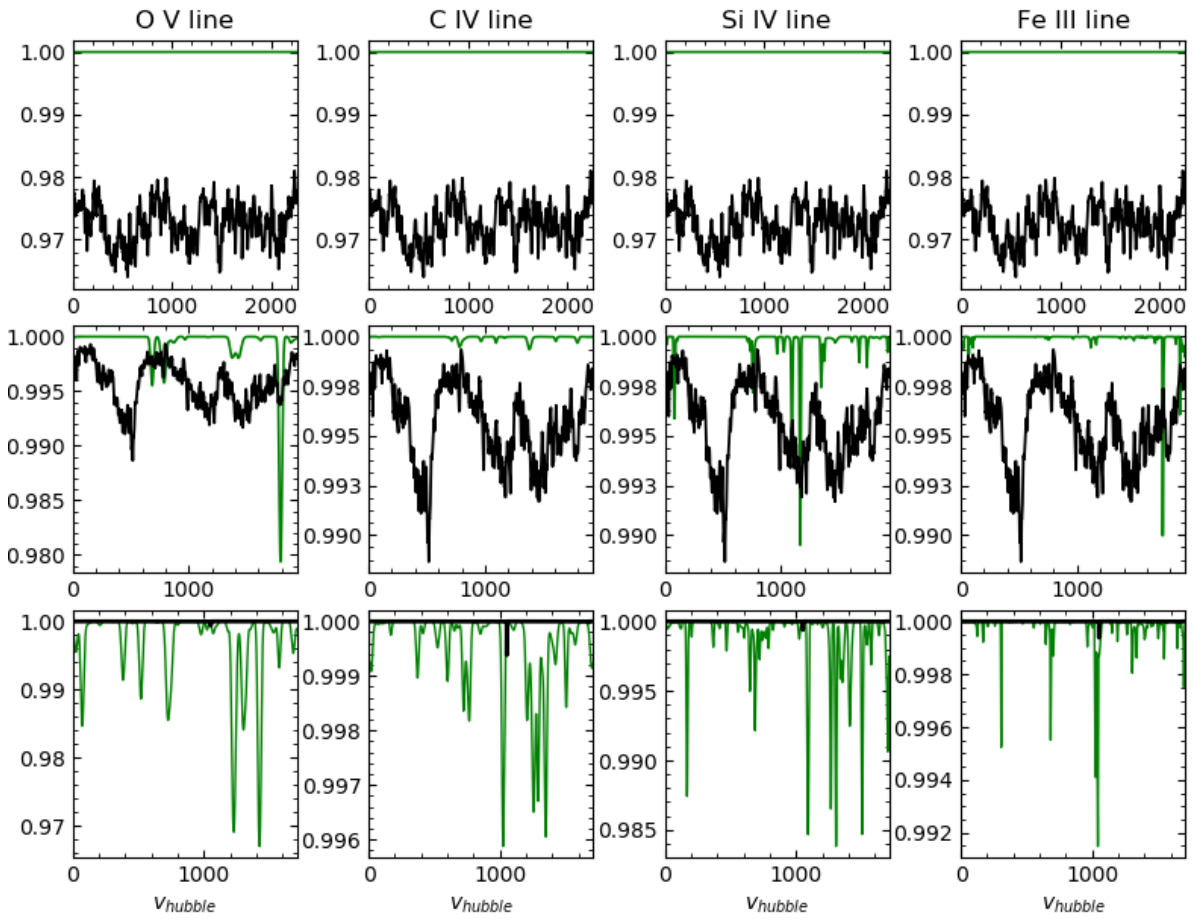

Figure 5.18: Stacked spectra at z = 11.32 (upper panels), 7.96 (middle panels) and 6 (lower panels) for high iononization states of metals specified at the top of the column (green line) and the stacked 21 cm absorpion spectrum (black line).

Chapter 6

Conclusions

Through the course of this study, we study the absorption from metals and 21 cm line of hydrogen as a probe of the IGM through reionization. We looked at the physical evolution of the IGM to see if the evolution allows for favourable conditions to sustain neutral hydrogen to produce absorption from the 21 cm line of neutral hydrogen. Then we looked at the metal enrichment history of IGM and properties of the metal rich IGM. We then proceed to derive synthetic spectra using prescriptions of optical depths for metals and the 21 cm forest. Then we studies the outputs using stacking random spectra and doing a statistical study of spectra in the metal rich regions. In this chapter I will summarize the results obtained and further plans for this study.

6.1 Is there enough absorption?

We derived spectra from 5000 lines of sight keeping in mind the difficulties to observe the universe at such high redshifts, this is a large number. From Fig. 5.6 we see the highest absorption from 21 cm is at $z = 8$. Number density distribution a tail of particles specially for the low ionization state metals, which suggests there should be enough absorption. In the distribution of optical depths, we showed that while there is absorption, the abundance of high optical depth systems is reduced by physical state of gas ($T \gg 10^4$).

6.2 Is metal and 21 cm absorption correlated?

The phase diagrams of the IGM that show the distribution of metallicity and the distribution of $e^{-\tau_{21cm}}$ vs $e^{-\tau_{metal}}$ do not show any strong correlations. Overdense IGM is usually metal eniched as star formation occurs in such regions, therefore metal rich IGM can have very high column densities of neutral hydrogen. As seen from the results above, we do see most metal rich IGM is highly neutral, but these regions are hot ($T \gg 10^4$). Hence in some of this gas, the 21 cm signal is suppressed because of high spin temperatures. However, as seen from the results, we could use metal absorption systems (both low and high ionization state) as tracers for IGM in a variety of physical states.

6.3 Is it observationally feasible?

The spectra that we have created are pure ie. noise free. Instrument effects and foreground effects contribute noise which can dominate the absorption signal. Hence, careful modelling of the instrument noise and foreground galactic/extragalacic noise will be of utmost importance for studies of 21 cm absorption as the absorption signal is expected to be weak. The metal absorption lines we studied have already been observed in the spectra of quasars and lyman alpha emitters in the EoR. We are in the process of creating mock observations of high redshift quasar spectra to see the observational feasibility of the 21 cm and metal forests and to see if a cross-correlation study of the same is feasible.

6.4 Future prospects

Studies such as this can provide us with invaluable information about the epoch of reionization. In the upcoming weeks we plan to do a detailed stacking study of spectra with better weighting schemes and follow that up by creating mock observations for some next generation telescopes such as the SKA. Other studies such as characterizing various absorption systems, the shape of the UV backgrounds, population III stars are also on the horizon using the metal and 21 cm absorption features.
Insights gained from metal absorption lines will be useful for analysis of data from various

future surveys of the high redshift universe. In summary, the prospects for expanding our understanding of the epoch of reionization are excellent in the near future.

Bibliography

[1] Barkana, R., and Loeb, A. In the beginning: the first sources of light and the reionization of the universe. *349* (Jul 2001), 125–238.

[2] Becker, G. D., Bolton, J. S., Madau, P., Pettini, M., Ryan-Weber, E. V., and Venemans, B. P. Evidence of patchy hydrogen reionization from an extreme lyα trough below redshift six. *Monthly Notices of the Royal Astronomical Society 447*, 4 (2015), 3402–3419.

[3] Chabrier, G. Galactic Stellar and Substellar Initial Mass Function. *115* (July 2003), 763–795.

[4] Dalla Vecchia, C., and Schaye, J. Simulating galactic outflows with thermal supernova feedback. *426* (Oct. 2012), 140–158.

[5] Ferland, G., Porter, R., Van Hoof, P., Williams, R., Abel, N., Lykins, M., Shaw, G., Henney, W., and Stancil, P. The 2013 release of cloudy. *Revista mexicana de astronomía y astrofísica 49*, 1 (2013), 137–163.

[6] Finkelstein, S. L., Dunlop, J., Fevre, O. L., and Wilkins, S. The case for a james webb space telescope extragalactic key project. *arXiv preprint arXiv:1512.04530* (2015).

[7] Furlanetto, S. R., and Loeb, A. Metal absorption lines as probes of the intergalactic medium prior to the reionization epoch. *The Astrophysical Journal 588*, 1 (2003), 18.

[8] Komatsu, E., Smith, K. M., Dunkley, J., Bennett, C. L., Gold, B., Hinshaw, G., Jarosik, N., Larson, D., Nolta, M. R., Page, L., Spergel, D. N., Halpern, M., Hill, R. S., Kogut, A., Limon, M., Meyer, S. S., Odegard, N., Tucker, G. S., Weiland, J. L., Wollack, E., and Wright, E. L. Seven-year Wilkinson Microwave Anisotropy Probe (WMAP) Observations: Cosmological Interpretation. *192* (Feb. 2011), 18.

[9] Lidz, A., Zahn, O., McQuinn, M., Zaldarriaga, M., and Hernquist, L. Detecting the rise and fall of 21 cm fluctuations with the murchison widefield array. *The Astrophysical Journal 680*, 2 (2008), 962.

[10] Mellema, G., Koopmans, L. V., Abdalla, F. A., Bernardi, G., Ciardi, B., Daiboo, S., de Bruyn, A., Datta, K. K., Falcke, H., Ferrara, A., et al. Reionization and the cosmic dawn with the square kilometre array. *Experimental Astronomy 36*, 1-2 (2013), 235–318.

[11] Oh, S. P. Probing the dark ages with metal absorption lines. *Monthly Notices of the Royal Astronomical Society 336*, 3 (2002), 1021–1029.

[12] Osterbrock, D. E., and Ferland, G. J. *Astrophysics Of Gas Nebulae and Active Galactic Nuclei*. University science books, 2006.

[13] Ota, K., Walter, F., Ohta, K., Hatsukade, B., Carilli, C. L., da Cunha, E., González-López, J., Decarli, R., Hodge, J. A., Nagai, H., et al. Alma observation of 158 μm [c ii] line and dust continuum of az= 7 normally star-forming galaxy in the epoch of reionization. *The Astrophysical Journal 792*, 1 (2014), 34.

[14] Pawlik, A. H., Milosavljević, M., and Bromm, V. The first galaxies: assembly under radiative feedback from the first stars. *The Astrophysical Journal 767*, 1 (2013), 59.

[15] Pawlik, A. H., Rahmati, A., Schaye, J., Jeon, M., and Dalla Vecchia, C. The Aurora radiation-hydrodynamical simulations of reionization: calibration and first results. *466* (Apr. 2017), 960–973.

[16] Pawlik, A. H., and Schaye, J. TRAPHIC - radiative transfer for smoothed particle hydrodynamics simulations. *389* (Sept. 2008), 651–677.

[17] Pawlik, A. H., and Schaye, J. Multifrequency, thermally coupled radiative transfer with TRAPHIC: method and tests. *412* (Apr. 2011), 1943–1964.

[18] Planck Collaboration, Ade, P. A. R., Aghanim, N., Arnaud, M., Ashdown, M., Aumont, J., Baccigalupi, C., Banday, A. J., Barreiro, R. B., Bartlett, J. G., and et al. Planck 2015 results. XIII. Cosmological parameters. *594* (Sept. 2016), A13.

[19] Raičević, M., Pawlik, A. H., Schaye, J., and Rahmati, A. The effect of recombination radiation on the temperature and ionization state of partially ionized gas. *437* (Jan. 2014), 2816–2830.

[20] Schaerer, D. The transition from Population III to normal galaxies: Lyalpha and He II emission and the ionising properties of high redshift starburst galaxies. *397* (Jan. 2003), 527–538.

[21] Schaye, J., and Dalla Vecchia, C. On the relation between the Schmidt and Kennicutt-Schmidt star formation laws and its implications for numerical simulations. *383* (Jan. 2008), 1210–1222.

[22] Schaye, J., Vecchia, C. D., Booth, C., Wiersma, R. P., Theuns, T., Haas, M. R., Bertone, S., Duffy, A. R., McCarthy, I., and van de Voort, F. The physics driving the cosmic star formation history. *Monthly Notices of the Royal Astronomical Society 402*, 3 (2010), 1536–1560.

[23] Semelin, B. Detailed modelling of the 21-cm forest. *455* (Jan. 2016), 962–973.

[24] Springel, V. The cosmological simulation code GADGET-2. *364* (Dec. 2005), 1105–1134.

[25] Theuns, T., Leonard, A., Efstathiou, G., Pearce, F. R., and Thomas, P. A. P^3M-SPH simulations of the Lyalpha forest. *301* (Dec. 1998), 478–502.

[26] Wiersma, R. P. C., Schaye, J., and Smith, B. D. The effect of photoionization on the cooling rates of enriched, astrophysical plasmas. *393* (Feb. 2009), 99–107.

[27] Wisotzki, L., Bacon, R., Blaizot, J., Brinchmann, J., Herenz, E. C., Schaye, J., Bouché, N., Cantalupo, S., Contini, T., Carollo, C. M., et al. Extended lyman α haloes around individual high-redshift galaxies revealed by muse. *Astronomy & Astrophysics 587* (2016), A98.

[28] Wolfe, A. M., Gawiser, E., and Prochaska, J. X. Damped Ly α Systems. *43* (Sept. 2005), 861–918.

[29] Zaroubi, S., De Bruyn, A., Harker, G., Thomas, R., Labropolous, P., Jelić, V., Koopmans, L., Brentjens, M., Bernardi, G., Ciardi, B., et al. Imaging neutral hydrogen on large scales during the epoch of reionization with lofar. *Monthly Notices of the Royal Astronomical Society 425*, 4 (2012), 2964–2973.